

ABSTRACT

WELLENIUS, PATRICK. Nitrogen Doping and Ion Beam Processing of Zinc Oxide Thin Films. (Under the direction of Dr. John Muth)

The modification of single crystal epitaxial ZnO thin films grown by Pulsed Laser Deposition on c-axis oriented sapphire substrates by Ion Beam Processing was investigated. Nitrogen doping of the films was attempted using nuclear transmutation using the $^{16}\text{O} (^3\text{He}, ^4\text{He}) ^{15}\text{O}$ reaction at 6.6 MeV. The ^{15}O product is unstable and decays to ^{15}N after several minutes by positron emission. There are several potential advantages to using nuclear transmutation including producing nitrogen atoms on the correct lattice site for doping and reduced crystal damage as compared to conventional ion beam implantation. In the experiments in this thesis the doping levels achieved $\sim 10^{14} \text{ cm}^{-3}$ were too low to be expected to dope the films to p-type. However several beneficial effects due to the ion beam processing were observed, including large increases in resistivity, reduction of defect luminescence, and substantial increases in the response of photoconductive detectors. In addition to desired effects in some films it was also found that in some films bubble like structures approximately 10 μm in diameter were formed where the thin film delaminated from the surface. It was assumed that mechanism for the bubble formation was the build up of helium gas at the sapphire/ZnO interface.

Nitrogen Doping and Ion Beam Processing of Zinc Oxide Thin Films

by

Patrick Wellenius

A thesis submitted to the Graduate Faculty of

North Carolina State University

In partial fulfillment of the
requirements for the degree of

Master of Science

in

Electrical Engineering

Raleigh, NC

2005

Approved by:

Professor John Muth
(Chair of Advisory Committee)

Professor Robert Kolbas

Professor Salah Bedair

BIOGRAPHY

Ian Patrick Wellenius was born on December 4th, 1981 in Potomac, Maryland. After graduating high school in May, 1999 from Washington International School in Washington, DC, Patrick went on to study Electrical Engineering at North Carolina State University; receiving a Bachelor of Science in May, 2003. An ongoing internship at the Naval Surface Warfare Center, beginning in 10th grade, guided Patrick's interests towards materials science. With that interest in mind, Patrick continued his academic career at NC State, receiving a Master of Science in Electrical Engineering in December, 2005 under the supervision of Dr. John Muth and with the extensive help of Dr. Jack Price and Dr. Noel Guardala.

ACKNOWLEDGMENTS

There are several people without whom, this work would not have come to fruition. I would first like to thank my parents and entire family for their continued love and support. I also wish to thank Dr. John Muth for his support and guidance over the last two years. Dr. Jack Price and Dr. Noel Guardala have been instrumental, not only in my research, but also in my development as a scientist and a professional. I am very grateful for their teachings and friendship over the past several years. I would also like to thank Joe Matthews, Daryl Fothergill, Brandon Conover, Anuj Dhawan, Roy Zhang, Ailing Cai, Hugh Porter, Jason Kekas and Christian Mion for their friendship and assistance over the past two years.

TABLE OF CONTENTS

LIST OF FIGURES	VI
LIST OF TABLES	VIII
<u>1</u>	<u>BACKGROUND.....1</u>
1.1	THE STATE OF ZNO AND TECHNOLOGY2
1.2	PULSED LASER DEPOSITION OF ZNO THIN FILMS6
1.3	DOPING BY NUCLEAR TRANSMUTATION.....7
1.4	SUMMARY12
1.5	REFERENCES13
<u>2</u>	<u>EXPERIMENTAL METHOD.....16</u>
2.1	PULSED LASER DEPOSITION OF ZNO THIN FILMS17
2.2	ANNEALING OF ZNO THIN FILMS.....20
2.3	ION BEAM TRANSMUTATION DOPING22
2.3.1	³ HE IRRADIATION OF ZNO THIN FILMS25
2.4	CHARACTERIZATION TECHNIQUES26
2.4.1	FOUR-POINT PROBE RESISTIVITY MEASUREMENTS27
2.4.2	LUMINESCENCE30
2.4.3	PHOTOCONDUCTIVITY32
2.4.4	RUTHERFORD BACKSCATTERING SPECTROMETRY36
2.4.5	NUCLEAR REACTION ANALYSIS.....39
2.5	REFERENCES40
<u>3</u>	<u>EXPERIMENTAL RESULTS FOR ZNO.....41</u>
3.1.1	PLD GROWTH OPTIMIZATION41
3.2	ANNEALING OF ZNO THIN FILMS.....43
3.2.1	TIME DEPENDENT ANNEALING43
3.2.1.1	Four-Point Probe44
3.2.1.2	Atomic Force Microscopy.....45
3.2.1.3	Rutherford Backscattering Spectrometry46
3.2.2	TEMPERATURE-DEPENDENT ANNEALING49
3.2.2.1	Resistivity49
3.2.2.2	Atomic Force Microscopy.....50
3.2.2.3	Rutherford Backscattering Spectrometry51
3.2.2.4	Luminescence.....55
3.3	³ HE IRRADIATION OF ZNO THIN FILMS56
3.3.1	SCANNING ELECTRON MICROSCOPY57
3.3.2	LUMINESCENCE60
3.3.3	RESISTIVITY61
3.3.4	ATOMIC FORCE MICROSCOPY62
3.3.5	PHOTOCONDUCTIVITY63
3.4	REFERENCES67

<u>4</u>	<u>CONCLUSIONS.....68</u>
4.1	PULSED LASER DEPOSITION OF ZNO THIN FILMS68
4.2	ANNEALING OF ZNO THIN FILMS.....69
4.3	³HE IRRADIATION OF ZNO THIN FILMS69
4.4	CONSIDERATIONS FOR FUTURE WORK.....70

LIST OF FIGURES

Figure 1.1 - Crystalline ZnO forms in the wurtzite structure.	3
Figure 1.3 - Implantation profile for 6.6 MeV ³ He ions into a ZnO on sapphire.....	10
Figure 1.4 - Collision distribution for 6.6 MeV ³ He ions onto a ZnO on sapphire	11
Figure 2.1 - Schematic of the pulsed laser deposition chamber.....	18
Figure 2.2 - Photographs of the PLD system and ablated ZnO inside the chamber	18
Figure 2.3 - Layout of the Positive Ion Accelerator Facility (PIAF)	23
Figure 2.4 - Schematic drawing of the 3 MV tandem accelerator used at the PIAF	24
Figure 2.5 - Photograph of the high-energy end of the accelerator at the PIAF.....	25
Figure 2.6 - Reaction cross sections for the competing transmutations.....	26
Figure 2.7 - A circuit schematic of the four-point probe apparatus	29
Figure 2.8 - Electronic transitions in semiconductors	30
Figure 2.9 - A comparison of standard and interdigitated contacts.	32
Figure 2.10 - RBS analysis on a target composed of two monatomic layers.	37
Figure 2.11 - Ideal spectra of a Au on Si target and a Au-Si alloy	38
Figure 3.1 - Effects of O ₂ partial pressure and temperature during deposition.	41
Figure 3.2 - CL and SEM imaging micrographs of ZnO nanostructures.....	42
Figure 3.3 - PL spectra demonstrating decreased defect luminescence.....	42
Figure 3.4 - FWHM of XRD for as-grown ZnO films as a function of temperature.....	43
Figure 3.5 - Plot of resistivity versus cumulative annealing time	44
Figure 3.6 - AFM micrographs of film surfaces: as-grown and after 3 hour anneal	45
Figure 3.7 - AFM micrographs of film surfaces: after 6 and 15 hours total anneal.....	46
Figure 3.8 - RMS roughness of a ZnO film after successive anneals in air.....	46

Figure 3.9 - RBS spectra of 3 films: one as-grown, and two annealed.....	47
Figure 3.10 - Stoichiometry profile for annealed ZnO films.....	48
Figure 3.11 - Plot of film resistivity against annealing temperature.....	50
Figure 3.12 - RMS roughness for ZnO films annealed at varying temperatures.	51
Figure 3.13 - AFM images comparing two annealed films.....	51
Figure 3.14 - Sample RBS spectrum from a thin ZnO film used in the RTA study	53
Figure 3.15 - RBS spectra show the change in oxygen content among annealed films.	53
Figure 3.16 - RBS spectra show the isotopic resolution achieved with high energies.	54
Figure 3.17 - Nitrogen-beam HIBS spectra of annealed films	55
Figure 3.18 - Changes in CL spectra after rapid thermal annealing.	56
Figure 3.19 - SEM micrograph of an irradiated ZnO film	57
Figure 3.20 - SEM and CL imaging micrographs of blisters formed on a ZnO film	59
Figure 3.21 - CL spectra depicting the annealing properties of the 3He ion beam.	60
Figure 3.23 - Interdigitated structures fabricated on ZnO films.....	64
Figure 3.24 - Resistivity and photoresponse in irradiated and unirradiated films.....	64
Figure 3.25 - Log(I)-V plot shows the response over several orders of magnitude	65
Figure 3.26 - Persistent photoconductivity effects observed in irradiated ZnO films.....	66

LIST OF TABLES

Table 1.1 - Group I and V acceptor properties in ZnO.....	4
Table 2.1 - Example conditions for PLD growth of various ZnO films.....	20
Table 2.2 - Example conditions for annealing of various ZnO films.....	21
Table 3.1 - Irradiation data and estimated dopant density for five ZnO films.....	56
Table 3.2 - RMS roughness for irradiated and unirradiated films.....	63

1 Background

Silicon has been the material of choice for integrated circuits and low power semiconductor electronic devices for the past 50 years. Scientists and engineers have studied and continue to push the limits of silicon technology meet the growing demand for advanced devices. Because of this long-standing history, silicon processing can be quite simple and inexpensive, and so it continues to be the material of choice for most applications.

Optoelectronic applications requiring light emission require the use of compound semiconductors with a direct bandgap. Traditionally this role has been dominated by GaAs, and InP compounds. More recently wide band gap semiconductor materials such as GaN or ZnO have been the subject of intense technical interest because with their wide band gap they can emit light in the visible and ultraviolet. This has resulted in commercialization of visible LEDs, blue and ultraviolet lasers and ultraviolet photodetectors. Wide band gap semiconductors are also increasingly being used in high power electronics such as solid state amplifiers and switches.

For extreme environments, such as outer space, radiation hardness can be a critical quality for devices since device performance can be significantly altered by the constant bombardment of energetic particles and electromagnetic radiation. Parameters such as threshold voltage, leakage current and saturation current that are critical to proper device performance may change significantly with a sufficient dose of ionizing radiation, which may cause equipment malfunction or failure. Materials such as ZnO or InP have been demonstrated to be more resistant to radiation damage than other semiconductors such as silicon and GaAs

1.1 The State of ZnO and Technology

ZnO is of particular interest due to its wide bandgap and excellent optical qualities, making it a promising material for several applications such as ultraviolet optoelectronics, transparent contacts, varistors and gas sensors. It is also nearly identical in lattice spacing to GaN, meaning that integration of ZnO with GaN based systems is possible.

The major difficulty in producing ZnO devices is the lack of p-type doping. As grown, ZnO is n-type due to structural defects from the growth process, such as oxygen vacancies, zinc interstitials and antisites. An antisite occurs when a nucleus of one species occupies a lattice site that is typically occupied by another species, such as a zinc nucleus on an oxygen site in the lattice. A vacancy is an unoccupied lattice site, resulting in unsatisfied bonds within the lattice. An interstitial defect is a nucleus that does not occupy a lattice site, perturbing the periodic potential that gives rise to the ideal band structure.

The ideal band structure of a semiconductor is born out of the periodicity of a crystal lattice, and the periodic electric potential associated with it. Any deviation from an ideal, periodic lattice will create distinct energy levels in the bandgap; as such deviations perturb the periodic potential. An ideal lattice is impossible to fabricate, so the objective of any film growth or deposition is to minimize the defect densities in the material, minimizing the intrinsic perturbations to the lattice

A ZnO crystal has the wurtzite structure (see figure 1.1). The large spheres represent the zinc nuclei and the smaller spheres represent the oxygen nuclei. In the wurtzite structure, a cation is bonded to four nearest neighbor anions and each anion is

similarly bonded with four cations. Thus each oxygen nucleus is bound to four zinc nuclei, and each zinc nucleus is bound to four oxygen nuclei.

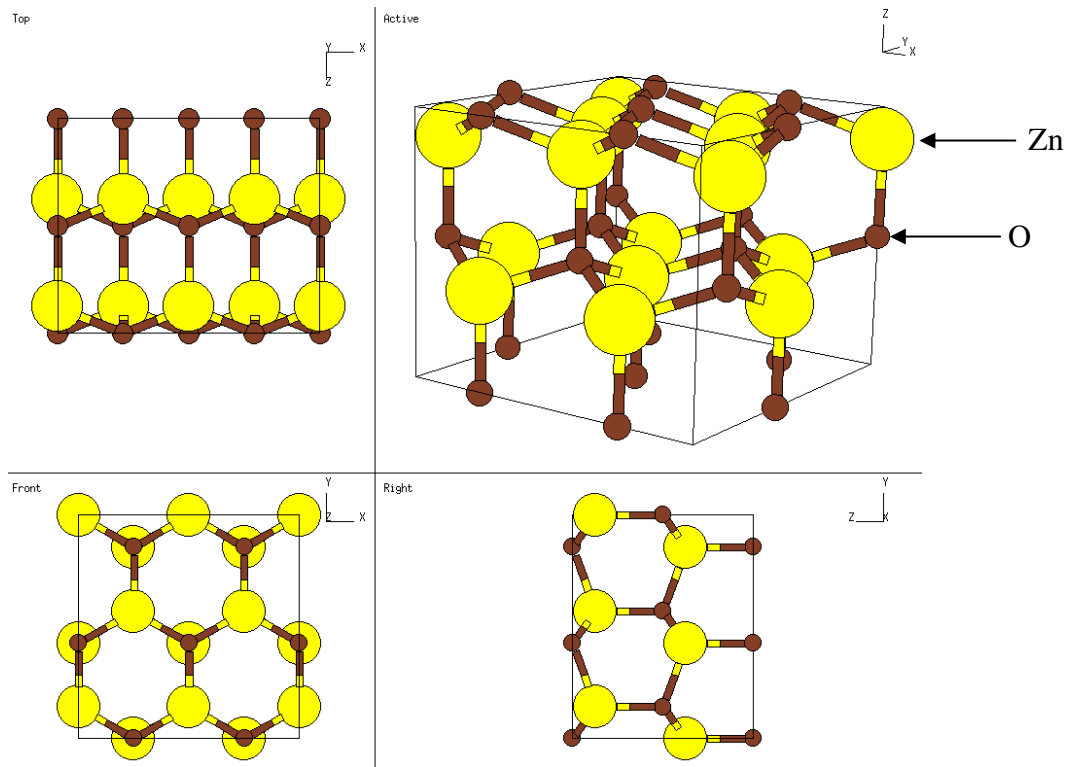


Figure 1.1 - Crystalline ZnO forms in the wurtzite structure, shown here from 4 different angles.¹

Production of quality p-type ZnO films has been problematic, mostly due to defects caused by dopant induced stresses in the crystal. Very low formation energies for oxygen vacancies and zinc interstitials in ZnO have been calculated and likely explain the native n-type conductivity observed in as-grown films². These low energy defects may also be the cause of n-type defects, causing the self-compensation observed for acceptors. Ultimately, this makes p-type doping very difficult.³ Of the possible acceptor species for ZnO, nitrogen is the favorite because the Zn-N bond (1.88 Å) is the most similar in length to the Zn-O bond it would replace (1.93 Å), as shown in table 1.1. Close matching of the

bond length reduces the crystal strain and thus, reduces the likelihood of compensating defect formation. For this reason, it is preferable to develop methods of doping ZnO films with nitrogen. However, recent reports have also indicated that phosphorus, arsenic, and even antimony can act as p-type dopants.

Table 1.1 – Group I and V acceptor properties in ZnO (adapted from Park, et al).

Dopant	Bond length (Å)	Calculated energy level (meV)	Group
Li	2.03	90	I
Na	2.10	170	I
K	2.42	320	I
N	1.88	400	V
P	2.18	930	V
As	2.23	1150	V

Determining the conductivity type of ZnO is experimentally difficult for several reasons including, low mobility, difficulty in making ohmic contacts, persistent photoconductivity effects and the formation of a degenerate surface layer. However, a number of authors have reported p-type behavior and their results are summarized below. At the present stage of development of ZnO, it is likely that some of these reports may be suspect due to the measurement and material-related issues listed above.

A typical method for producing p-type ZnO by PLD is to ablate a target where the dopant is incorporated in the desired stoichiometry. This technique, or variations thereof, was used to attempt growth of p-type ZnO doped with phosphorus^{4,5,6} with mixed results. Hall mobilities were consistently low for p-type material, ranging from 1 to 40 cm²/Vs, or were ambiguous and inconsistent. Resistivities also varied from 1 to 330 Ω-cm.

Arsenic doped ZnO has been demonstrated by low-temperature ion implantation, using a short *in-situ* anneal. The authors reported having produced p-type ZnO, but samples again demonstrated very low Hall mobility, ranging from approximately 1 to 7

cm²/Vs, despite having low p-type carrier concentrations.⁷ A similar study used GaAs substrates as the source of arsenic dopants where films prepared by PLD at 400 and 450 °C demonstrated p-type conductivity. The Hall mobility for the p- and n-type films was in the range of 0.1-50 cm²/Vs and 1-50 cm²/Vs, respectively.⁸

ZnO films p-type doped with lithium and antimony were most recently reported and the Hall effect measurements are consistent throughout the materials used in the study. While the various lithium-doped films were repeatedly characterized as having p-type conductivity, the Hall mobilities were between 0.3 and 4 cm²/Vs, with resistivities ranging from 17 Ω-cm up to 73 kΩ-cm.⁹ Antimony-doped films demonstrated p-type conductivity, Hall mobilities between 20 and 25 cm²/Vs and resistivities between 0.2 and 0.3 Ω-cm.¹⁰

Assorted co-doping strategies have been implemented in hopes of producing p-type material as well. One recent study used aluminum and nitrogen to co-dope ZnO on glass, quartz, sapphire and conductive Si (10⁻³ Ω-cm) substrates and demonstrated results similar to mono-doped films. Except for the films deposited on silicon, the resistivities were between 2 and 57 Ω-cm and Hall mobilities between 0.4 and 1.6 cm²/Vs. Samples consistently demonstrated p-type conductivity. The films grown on silicon demonstrated a much higher mobility (159 cm²/Vs) and much lower resistivity (0.029 Ω-cm) but this is because the current is not confined to the ZnO film with the conducting substrate as it is with an insulating substrate.¹¹

Another study co-doped ZnO with tellurium and nitrogen. A major difference between these two studies is that aluminum is a simple donor in II-VI compounds, whereas tellurium is isoelectronic, meaning it has the same valence as the group II

elements it would displace as a dopant. The purpose of doping ZnO with tellurium prior to doping with nitrogen is to make a more suitable host for the nitrogen acceptors. The study showed that ZnO:Te films were slightly p-type, prior to doping with nitrogen and that co-doped films were increasingly p-type. Co-doping of the films caused a resistivity increase over several orders of magnitude from 10^{-2} to 10^5 Ω -cm and substantial improvement in spectrally dependent photoconductivity measurements.¹²

1.2 Pulsed Laser Deposition of ZnO Thin Films

ZnO films can be grown by pulsed laser deposition (PLD) whereby a pressed and sintered ZnO target is ablated using high energy laser pulses and the ablated material is deposited onto a heated substrate.¹³ PLD produced wide bandgap films have been previously used for metal-semiconductor-metal (MSM) photoconductive UV detectors.¹⁴ Qualitative and quantitative material parameters can be extracted from the performance of these devices, making them ideal for a fundamental study. Bulk film properties can also be studied using room- and low-temperature photoluminescence (PL) methods as well as X-Ray Diffraction.

Naturally grown ZnO films are usually n-type and have low to moderate resistivities due to the high native carrier concentrations. High quality photodetectors generally require highly resistive films, as this produces a greater contrast between light and dark currents. To achieve resistive, optical quality films the growth and annealing conditions must first be optimized. Studies have shown that films grown at higher substrate temperatures have a greater crystallinity, better surface morphology and higher resistivity¹⁵. It has also been shown that higher oxygen partial pressure during deposition

tends to produce more resistive films¹⁶. This is attributed to the improved stoichiometry of the film. However, the higher growth temperatures and higher oxygen pressures have also been shown to have an adverse effect on film morphology. Thus the proper parameter space for thin film growth for a particular growth reactor should be explored.

As p-type doping continues to be a difficulty in ZnO device fabrication and IBNTD may introduce a successful alternative. Furthermore, ZnO has been reported to be radiation-hard and what damage does occur can be annealed easily, making it an ideal candidate for this transmutation study.^{17,18} It has been suggested that the exceptional resistance to radiation is due to extraordinarily strong defect annihilation in ZnO films.¹⁹

1.3 Doping by Nuclear Transmutation

Transmutation doping uses nuclear reactions to transmute target nuclei from one atomic species to another, rather than displacing nuclei by implantation. A similar process has been used for bulk doping Si wafers using neutrons, called neutron transmutation doping (NTD). If applied to ZnO, IBNTD could be used to produce p-type films doped with nitrogen. A ^3He beam at 6.6 MeV impinging on the film will transmute ^{16}O to ^{15}O by alpha particle emission (see figure 1.3). The reaction product then decays to ^{15}N with a half-life of 122 seconds by positron emission. A simultaneous reaction occurs at similar energies that transmutes ^{16}O to ^{18}F , emitting a proton, followed by positron emission to ^{18}O with a half-life of approximately 110 minutes.²⁰ 37 hours after exposure, the ^{18}F population decays exponentially to one millionth of its maximum value.

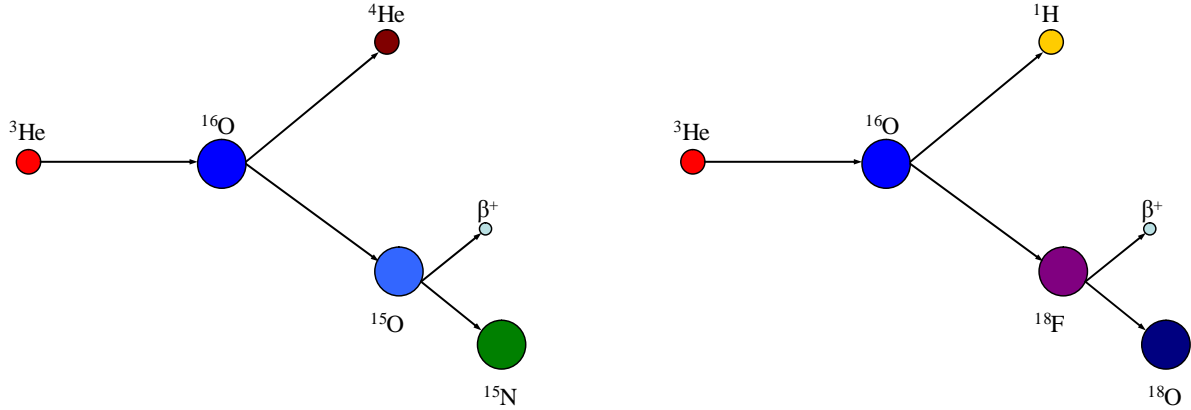


Figure 1.2 – A schematic representation of the major competing transmutations at 6.6 MeV: $^{16}\text{O}(^3\text{He}, ^4\text{He})^{15}\text{O}$ (left) and $^{16}\text{O}(^3\text{He}, \text{p})^{18}\text{F}$ (right). Products from both reactions decay by positron emission to produce ^{15}N and ^{18}O , respectively.

Because IBNTD uses light ion beams to cause a nuclear reaction in the target, scattering induced damage is potentially reduced. By minimizing lattice damage, annealing requirements can be reduced in fabrication processes. That would simplify processes for all electronic materials, but is even more important for wide bandgap semiconductors, which typically anneal at much higher temperatures.

Ion implantation is, by definition, a destructive process. Doping is achieved via the displacement of lattice nuclei using ions in the 100 keV to 1 MeV range. The implanted ions may or may not be substitutional once they come to a stop and along the way have caused numerous scattering events, resulting in nuclei displacement and lattice deformation. The energy absorbed by the lattice is linked to the mass and energy of the incident ion by equation 1.1.

$$\frac{E_2}{E_0} = 1 - \left[\frac{\sqrt{M_2^2 - M_1^2 \text{Sin}^2 q} + M_1 \text{Cos} q}{M_2 + M_1} \right]^2 \quad (1.1)$$

E_2 is the recoil energy of the lattice nuclei, M_2 is the mass of the lattice nuclei, E_0 is the initial energy of the impinging ion, M_1 is the impinging ion mass and θ is the scattering angle.²¹

IBNTD may cause considerably less lattice deformation than implantation because it utilizes a much smaller incident ion than implantation techniques. In implantation, ions which do not displace a nucleus still cause considerable damage by scattering through the lattice. In IBNTD, a light ion which does not cause a transmutation does much less scattering damage because of its significantly lower mass. Due to the high energy of the incident particles, coulombic interaction likely does not occur as it would at lower energies. As such, the majority of the ion-beam induced damage will be located at the end of the range, several microns deep. For thin film samples, this will occur well into the substrate. Damage to the film itself is limited to broken bonds, caused by energetic reaction products, including the emitted particle and the transmuted nucleus.

A simulation of a 6.6 MeV ^3He ion beam incident on a 500 nm ZnO film illustrates the elastic interactions of the ions with the target lattice. The simulation is calculated by a program called SRIM 2003 (The Stopping and Range of Ions in Matter), developed by J.F. Ziegler and J.P. Biersack. The results show that the implantation range of the ^3He ions is approximately 23 μm (see figure 1.4) and that most of the elastic scattering events occur well into the sapphire substrate, rather than in the ZnO film (see figure 1.5). The number of scattering events in the ZnO film much smaller than those occurring in the substrate, both in absolute terms as well as per unit thickness.

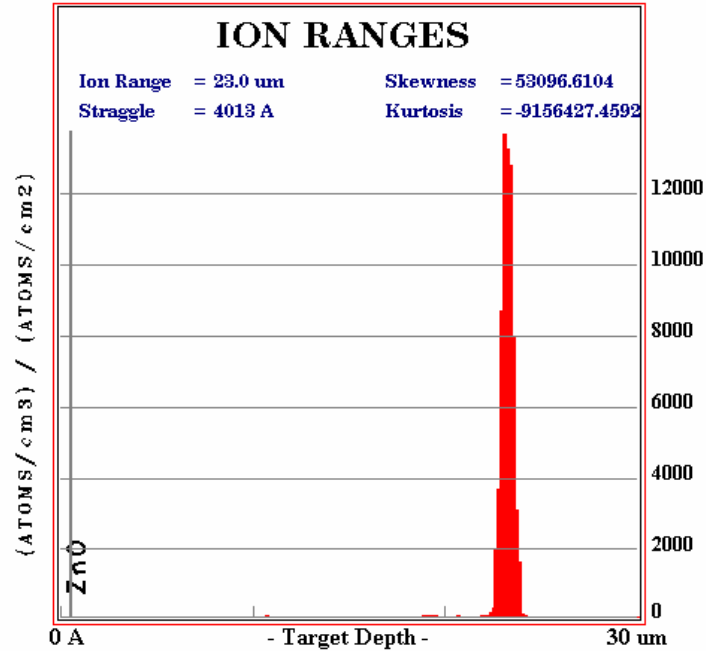


Figure 1.3 – Implantation profile for a 6.6 MeV ³He beam into a 500 nm ZnO film on sapphire, calculated by SRIM 2003. The implantation range of the ions is approximately 23 um; far away from the interface region.

The number of collision events is indicative of the number of vacancies produced by the incident ion beam. However, this number of vacancies is calculated assuming the irradiation is carried out at 0 K. Irradiating at 300 K often allows annealing to occur through self-heating.²² The nucleus recoil energy can be determined from the beam energy, Q-value and reaction product energy for a given scattering angle. This relationship is given by equation 1.2.

$$E_4 = E_1 + Q - E_3 \quad (1.2)$$

E_4 is the recoil energy of the heavy product (transmuted nucleus), E_1 is the energy of the incident ion, E_3 is the energy of the light product (e.g., emitted alpha particle) and

Q is the mass difference in the reaction. The mass difference is listed with other reaction parameters in nuclear datasets.

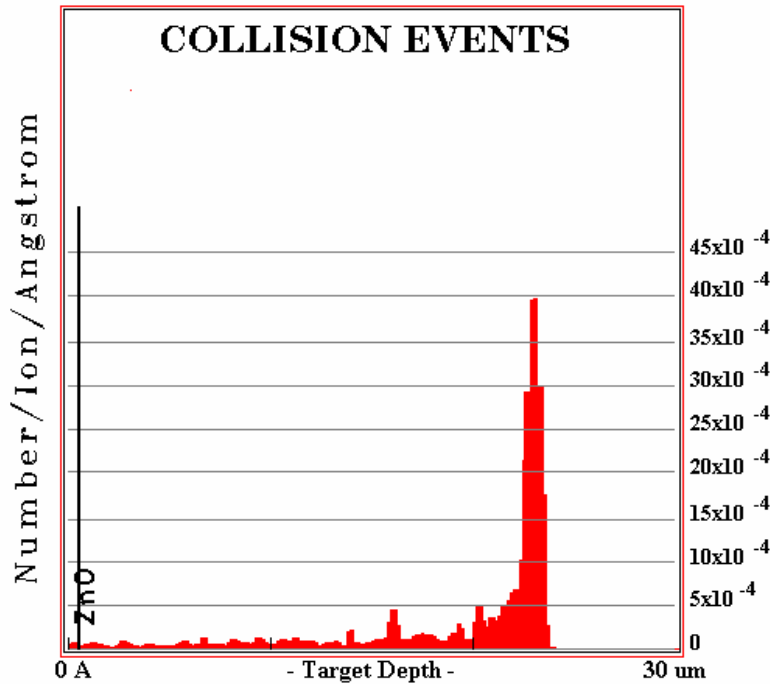


Figure 1.4 - Elastic collision distribution for a 6.6 MeV 3He ion beam into 500 nm ZnO film on sapphire, calculated by SRIM 2003. The vast majority of the events occur deep into the sapphire substrate, as opposed to the ZnO film.

In summary, due to its unique properties, ZnO is a desirable material for many specialized applications including UV optoelectronics, gas sensing, varistors and transparent contacts. ZnO technology has progressed significantly in recent years, resulting in the development of ZnO light emitting diodes and field effect transistors that often use p-type GaN in a heterojunction device. Problems exist which hinder the advancement of such devices, especially the difficulty in producing quality p-type films. Overcoming this major hurdle would enable the development of homojunction ZnO devices. Ion beam nuclear transmutation is an alternate method for doping ZnO that may

be a solution to this problem. As such, IBNTD requires attention and further study as a possible alternative for doping ZnO.

1.4 Summary

In this thesis we focus on studying ZnO as potential material for optoelectronic devices. Several experiments were conducted to determine the effects of film deposition conditions, annealing parameters and irradiation with ^3He ions on ZnO thin film characteristics. To this end, films were characterized by photoluminescence (PL), cathodoluminescence (CL), photoconductivity, four-point resistivity probe, scanning electron microscopy (SEM), atomic force microscopy (AFM), Rutherford backscattering spectrometry (RBS) and nuclear reaction analysis (NRA).

Pulsed laser deposition conditions were optimized by varying the substrate temperature and oxygen partial pressure during film growth. The number and energy of the laser pulses were fixed. Films were characterized by photoluminescence, resistivity and AFM to measure the optical, electrical and surface properties of the films with the goal being to achieve smooth, resistive films with low defect densities.

Two annealing studies were conducted. The first varied the annealing time, keeping a constant environment and temperature and the second varied the annealing temperature, keeping a constant environment and duration. Films from both studies were characterized by resistivity, AFM and RBS and the second study also included CL measurements. RBS analysis was utilized to determine both the stoichiometry and atomic distribution of zinc and oxygen in the films. The goal for these studies was to

observe the annealing behavior of ZnO thin films and optimize the annealing process to further maximize resistivity and luminescence behavior.

Irradiated films were characterized by CL, AFM, SEM, NRA and photoconductivity measurements to determine the efficiency of the transmutation process as a doping method as well as to study the side effects caused by the ion beam. The goal was to achieve p-type conductivity, or behavior that may reflect p-type compensation in the films.

1.5 References

-
- ¹ "The Wurtzite (B4) Structure," vol. 2005, pp. 1, 10/21. 2001 <http://cst-www.nrl.navy.mil/lattice/struk.picts/b4.s.png>
- ² F. Oba, S.R. Nishitani, S. Isotani, H. Adachi and I. Tanaka, "Energetics of native defects in ZnO," *J.Appl.Phys.*, vol. 90, pp. 824-828, JUL 15. 2001.
- ³ C.H. Park, S.B. Zhang and S.H. Wei, "Origin of p-type doping difficulty in ZnO: The impurity perspective," *Phys.Rev.B*, vol. 66, pp. 073202, AUG 15. 2002.
- ⁴ S.J. Pearton, D.P. Norton, K. Ip, Y.W. Heo and T. Steiner, "Recent progress in processing and properties of ZnO," *Prog.Mater.Sci.*, vol. 50, pp. 293-340, MAR. 2005.
- ⁵ V. Vaithianathan, B.T. Lee and S.S. Kim, "Pulsed-laser-deposited p-type ZnO films with phosphorus doping," *J.Appl.Phys.*, vol. 98, pp. 043519, AUG 15. 2005.
- ⁶ J.R. Duclere, R. O'Haire, A. Meaney, K. Johnston, I. Reid, G. Tobin, J.P. Mosnier, M. Guilloux-Viry, E. McGlynn and M.O. Henry, "Fabrication of p-type doped ZnO thin films using pulsed laser deposition," *J.Mater.Sci.-Mater.Electron.*, vol. 16, pp. 421-427, JUL. 2005.
- ⁷ G. Braunstein, A. Muraviev, H. Saxena, N. Dhere, V. Richter and R. Kalish, "P Type Doping of Zinc Oxide by Arsenic Ion Implantation," *Appl.Phys.Lett.*, vol. 87, pp. 192103, NOV 7. 2005.
- ⁸ Y.R. Ryu, S. Zhu, D.C. Look, J.M. Wrobel, H.M. Jeong and H.W. White, "Synthesis of p-type ZnO films," *J.Cryst.Growth*, vol. 216, pp. 330-334, JUL. 2000.

-
- ⁹ Y.J. Zeng, Z.Z. Ye, W.Z. Xu, L.L. Chen, D.Y. Li, L.P. Zhu, B.H. Zhao and Y.L. Hu, "Realization of p-type ZnO films via monodoping of Li acceptor," *J.Cryst.Growth*, vol. 283, pp. 180-184, SEP 15. 2005.
- ¹⁰ F.X. Xiu, Z. Yang, L.J. Mandalapu, D.T. Zhao, J.L. Liu and W.P. Beyermann, "High-mobility Sb-doped p-type ZnO by molecular-beam epitaxy," *Appl.Phys.Lett.*, vol. 87, pp. 152101, OCT 10. 2005.
- ¹¹ J.G. Lu, L.P. Zhu, Z.Z. Ye, F. Zhuge, B.H. Zhao, J.Y. Huang, L. Wang and J. Yuan, "p-type ZnO films by codoping of nitrogen and aluminum and ZnO-based p-n homojunctions," *J.Cryst.Growth*, vol. 283, pp. 413-417, OCT 1. 2005.
- ¹² H.L. Porter, A.L. Cai, J.F. Muth and J. Narayan, "Enhanced photoconductivity of ZnO films Co-doped with nitrogen and tellurium," *Appl.Phys.Lett.*, vol. 86, pp. 211918, MAY 23. 2005.
- ¹³ A. Ohtomo and A. Tsukazaki, "Pulsed laser deposition of thin films and superlattices based on ZnO," *Semicond.Sci.Technol.*, vol. 20, pp. S1-S12, APR. 2005.
- ¹⁴ R. Ghosh, B. Mallik, S. Fujihara and D. Basak, "Photoluminescence and photoconductance in annealed ZnO thin films," *Chem.Phys.Lett.*, vol. 403, pp. 415-419, FEB 25. 2005.
- ¹⁵ J.N. Zeng, J.K. Low, Z.M. Ren, T. Liew and Y.F. Lu, "Effect of deposition conditions on optical and electrical properties of ZnO films prepared by pulsed laser deposition," *Appl.Surf.Sci.*, vol. 197, pp. 362-367, SEP 30. 2002.
- ¹⁶ J.L. Zhao, X.M. Li, J.M. Bian, W.D. Yu and X.D. Gao, "Structural, optical and electrical properties of ZnO films grown by pulsed laser deposition (PLD)," *J.Cryst.Growth*, vol. 276, pp. 507-512, APR 1. 2005.
- ¹⁷ F.D. Auret, S.A. Goodman, M. Hayes, M.J. Legodi, H.A. van Laarhoven and D.C. Look, "Electrical characterization of 1.8 MeV proton-bombarded ZnO," *Appl.Phys.Lett.*, vol. 79, pp. 3074-3076, NOV 5. 2001.
- ¹⁸ R. Khanna, K. Ip, K.K. Allums, K. Baik, C.R. Abernathy, S.J. Pearton, Y.W. Heo, D.P. Norton, F. Ren, R. Dwivedi, T.N. Fogarty and R. Wilkins, "Effects of high dose proton irradiation on the electrical performance of ZnO Schottky diodes," *Phys.Status Solidi A-Appl.Res.*, vol. 201, pp. R79-R82, SEP. 2004.
- ¹⁹ C. Coskun, D.C. Look, G.C. Farlow and J.R. Sizelove, "Radiation hardness of ZnO at low temperatures," *Semicond.Sci.Technol.*, vol. 19, pp. 752-754, JUN. 2004.
- ²⁰ R.L. HAHN and E. RICCI, "Interactions of 3He Particles with 9Be 12C 16O and 19F," *Physical Review*, vol. 146, pp. 650-&, 1966.

²¹ W.K. Chu, J.W. Mayer and M.A. Nicolet, *Backscattering Spectrometry*, New York: Academic Press, 1978, p. 23

²² J.F. Ziegler, "SRIM Lab #2: Target Damage," vol. 2005, pp. 6, 3/21/2005
<http://www.srim.org/SRIM/Tutorials/SRIM%20Tutorial-2%20-%20Damage.pdf>

2 Experimental Method

This study was the result of a collaborative effort between the Nanoelectronics and Photonics group at North Carolina State University and the Positive Ion Accelerator Facility at the Naval Surface Warfare Center, Carderock Division in West Bethesda, MD. Film depositions, annealing and most characterizations were carried out at NCSU while ion beam analysis and irradiation was executed at the PIAF.

To best determine the effectiveness of IBNTD as a doping method for ZnO, low n-type concentrations need to be achieved in films prior to irradiation. For this study, several films were grown at varying oxygen partial pressures and substrate temperatures. The films were subsequently analyzed for high resistivity, defect levels and smooth surface morphology by four-point probe, PL and AFM. The sheet resistivity and RMS roughness of the films were quantitative figures of merit. Once the deposition process was optimized, several films were annealed in air at high temperature for varying times to determine the optimal annealing conditions. Annealed samples were characterized by four-point probe, PL, AFM and RBS to further examine resistivity, defects, surface properties and film stoichiometry.

The ZnO films were irradiated at the PIAF using a 6 MeV ^3He beam to produce the reaction, $^{16}\text{O}(^3\text{He}, ^4\text{He})^{15}\text{O}$, where the oxygen product decays with an approximate half-life of 2 minutes to ^{15}N , effectively replacing oxygen nuclei with nitrogen nuclei. The reaction $^{16}\text{O}(^3\text{He}, \text{p})^{18}\text{F}$ also occurs at similar energies, but produces an unstable isotope of fluorine which decays to ^{18}O with a half-life of 110 minutes. 20 half-lives

(approximately 37 hours) after exposure, the fluorine population has decayed to one-millionth of its peak level.

Irradiated films were studied by AFM, SEM, PL, TLM, photoconductivity and nuclear profiling as well as analysis of the nuclear products during irradiation. Films were also annealed and characterized after irradiation to determine the stable effects of the process

2.1 Pulsed Laser Deposition of ZnO Thin Films

ZnO deposition and characterization was performed at North Carolina State University's Nanoelectronics and Photonics Laboratory in Raleigh, NC. The films were grown using a Neocera Pulsed Energy Deposition system (see figures 2.1 and 2.2), capable of ablating targets by either pulsed laser or electron beams. The KrF excimer laser is typically operated at 23.6 kV, with an estimated power density of 4 J/cm^2 per pulse. Pulse duration is between 10 and 50 ns.

Sapphire is used as a substrate for the ZnO films deposited in these experiments. Substrates are cleaned thoroughly using heated solvents and then affixed to the holder using silver paste. A substrate is initially degreased after being diced by submerging it for several minutes each in a series of boiling solvents, including trichloro-ethylene followed by acetone and methanol. The substrate is then cleaned once more immediately before loading into the chamber by submerging it in boiling acetone and methanol for several minutes each, followed by a nitrogen stream to dry the sample. The substrate is attached to the holder immediately following the cleaning procedure to ensure the cleanest possible substrate. This is done by applying a small dot of silver paste on the

sample holder and pressing the substrate onto the paste. The holder with substrates is heated for several minutes on a hot plate to cure the paste. Once a clean substrate is firmly affixed to the holder, the assembly is loaded back into the PLD chamber.

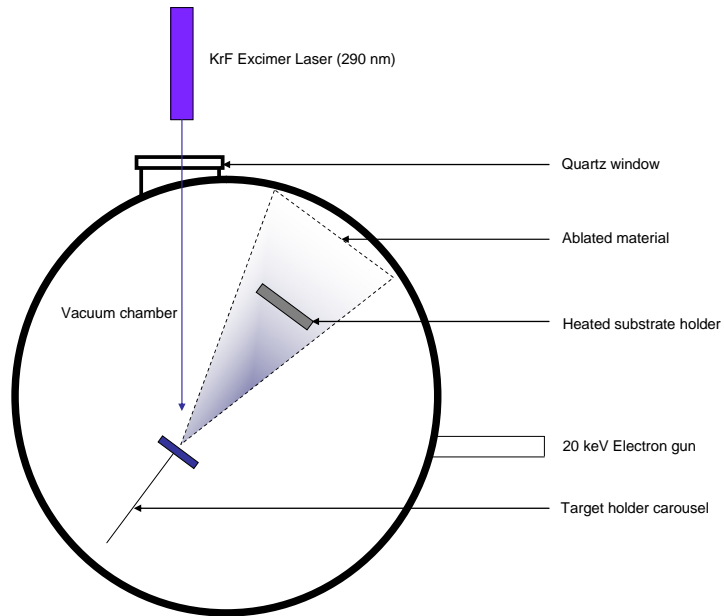


Figure 2.1 - Schematic drawing of the pulsed laser deposition chamber, including pulsed excimer laser and electron gun.

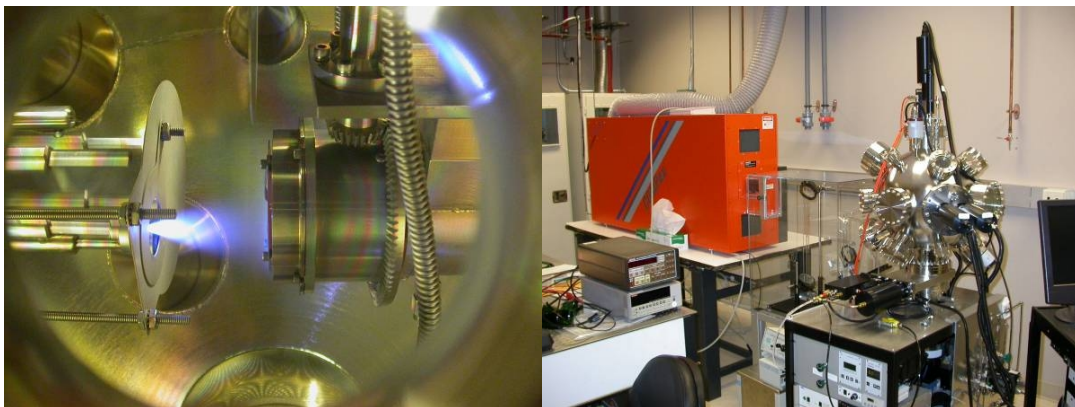


Figure 2.2 - Photographs of (a) the ablated ZnO material inside of the PLD chamber and (b) the PLD apparatus, including the excimer laser and vacuum chamber.

After reloading the sample holder, the PLD chamber is evacuated by means of a diaphragm roughing pump and a high speed turbomolecular (turbo) pump to a base pressure of approximately 5×10^{-7} Torr. The evacuated chamber may then be operated with a partial pressure of a specific ambient such as O₂ or argon gas, which are controlled individually using mass flow controllers. Chamber pressure is regulated via a feedback-loop operated gate valve, allowing for precise control over chamber pressure, ranging from 10^{-7} Torr up to approximately 100 mTorr.

Once the chamber reaches the desired pressure and ambient, the substrate is covered by a metal shutter and the laser is aligned to the target, which is rastered and rotated during deposition to minimize target pitting. After alignment, the target is pre-cleaned using several laser pulses. This helps to remove the very top surface under a controlled environment, providing clean material for ablation and film deposition. After the pre-clean, the substrate shutter is raised and the deposition can begin once the substrate reaches the desired temperature.

The temperature controller is used to pre-heat the substrate and holder to 950 °C to encourage out-gassing. Since the deposition is typically done around 700 to 800 °C, this high temperature pre-heating will drive off any moisture and other gaseous impurities in the substrates prior to deposition, rather than during. The substrate holder is capable of rotating at various speeds, to improve spatial uniformity, and boasts a programmable heating element used during growths and post-growth anneals, operating at room temperature and up to 1000 °C.

Several ZnO thin films were grown on c-plane sapphire by PLD under varying conditions (table 2.1). Studies have suggested that as-grown ZnO is typically n-type due

to several crystal defects, the most common of which is oxygen vacancy. This defect is responsible for high electron concentration and low electrical resistivity in unintentionally doped films. The vacancy concentration in ZnO films grown by PLD has been shown to have a strong correlation to the substrate temperature and oxygen partial pressure during deposition.^{1,2} After growth, the films were characterized to determine the optimal deposition conditions.

Table 2.1 - Example conditions for PLD growth of various ZnO films.

Film	Substrate temperature (degrees F)	O₂ Partial Pressure (mTorr)
ZnO_0429	700	1
ZnO_0505	800	1
ZnO_0516	900	1
ZnO_0524	750	5
ZnO_0525	750	25
ZnO_0526	750	35
ZnO_0606	800	35
ZnO_0608	700	35
ZnO_0609	700	35
ZnO_0612	700	35

2.2 Annealing of ZnO Thin Films

As-grown films grown under optimal conditions were annealed in air using a tube furnace at 800 °C, for varying times to characterize the time-dependent annealing effects (see table 2.2). Measurements were taken at different time intervals to quantify annealing effects using resistivity, luminescence and Atomic Force Microscopy methods. Further studies on certain samples were carried out using Rutherford Backscattering Spectrometry to observe changes in film stoichiometry with respect to annealing times.

Table 2.2 - Example conditions for annealing of various ZnO films.

Film	Temp (°C)	Total Time (hrs)	Ambient/method
ZnO_0612	800	4	In chamber, 35 mTorr O ₂
ZnO_0603	800	15	Quartz tube furnace, measurements made at 3,6, and 15 hours of total time.
ZnO_0608c	800	40	Quartz tube furnace

A second set of ZnO films were annealed for a given time under different temperatures, using an AG Associates HeatPulse 610 Rapid Thermal Annealer. Using this technique, it is possible to determine activation energies and diffusion coefficients for zinc and oxygen through ZnO. Such a study would provide significant insight into the mechanisms involved in annealing ZnO films.

RBS provides a quantitative profile of constituent atoms in a lattice, such as Zinc and oxygen in ZnO. Studying how the profile changes with respect to temperature provides a means to extract activation energies and diffusion coefficients. The diffusion coefficient for self-diffusion in a mono-atomic lattice is given by equation 2.1.

$$D_{SD} = D_0 e^{-\left(\frac{H_M + H_F}{kT}\right)} \quad (2.1)$$

D_0 is a pre-exponential factor containing the individual entropies, H_M and H_F are migration and formation entropies, k is Boltzmann's constant and T is the temperature.³

Using the above relationship, an Arrhenius plot ($\ln(D)$ versus reciprocal temperature)

can be used to determine the pre-exponential factor (the y-axis intercept) and the sum of H_M and H_F (the slope of the line).

2.3 Ion Beam Transmutation Doping

This study was carried out with the help of the Positive Ion Accelerator Facility (PIAF) at the Naval Surface Warfare Center, Carderock Division (NSWCCD) in West Bethesda, MD. The 3 MV NEC tandem pelletron accelerator uses two ion sources, is equipped with five experimental beam lines and features a 90 degree analyzing magnet to minimize energy dispersion in the beam (see figure 2.3).

The two ion sources can produce virtually any desired ion beam. The Alphasross ion source uses a 100 MHz RF oscillator to form plasma from hydrogen, helium or ammonia gas. This plasma produces proton, alpha particle or nitrogen ion beams. The SNICS (Source of Negative Ions by Cesium Sputtering) source uses interchangeable cathodes to produce beams of nearly any heavy ion, by sputtering material from the cathode using Cs atoms. Beam shaping and steering is achieved through several electromagnetic quadrupole lenses and electrostatic steerers respectively, located throughout the beam line.

A 90 degree analyzing magnet, controlled by a nuclear magnetic resonance (NMR) teslameter, defines the mass-energy of the ion beam. The analyzing magnet is similar in principle to a mass spectrometer in that the field strength is set to match a predetermined ion charge, mass and energy. This prevents other accelerated ions from being transmitted to the target at the end of the experimental beam lines. The energy resolution is approximately 2 keV, measured with a 1 MeV proton beam.

The experimental beam lines provide a versatile array of detectors and chambers, allowing one to carry out several common ion beam analysis techniques. The 30 degree left beam line is equipped with a scattering chamber, housing an x-ray detector and two particle detectors: one fixed at 150 degrees and one moveable. This line is commonly used for Rutherford backscattering spectrometry (RBS) and particle induced x-ray emission (PIXE). To facilitate operations, the 30 degree left beam line is also equipped with a set of electrostatic steerers which can be used to locate the beam on a specific location, or sweep the beam over a broad area.

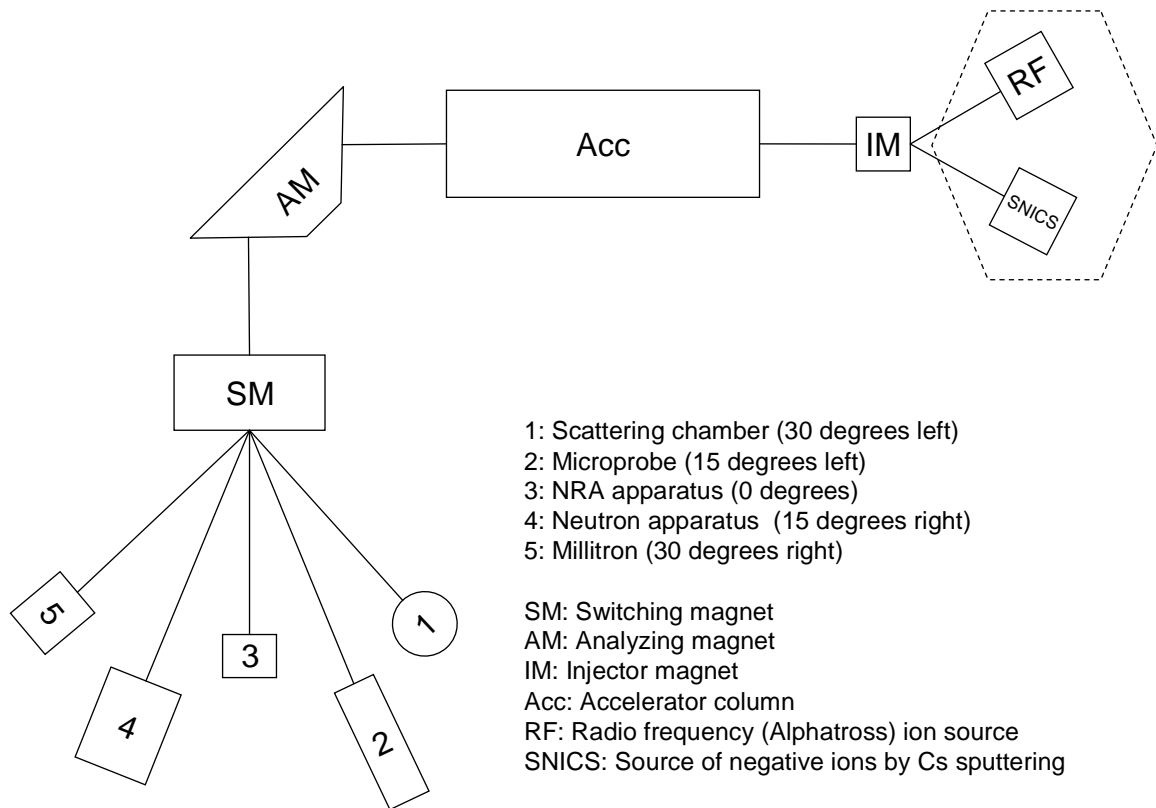


Figure 2.3 - Layout of the Positive Ion Accelerator Facility (PIAF) used for ion beam analysis and transmutation doping of ZnO films. The PIAF is a part of the Naval Surface Warfare Center Carderock Division.

Positioned at the 15 degree left beam line is a custom made microprobe, which can produce a beam as small as 25 microns in diameter. This beam can be used under vacuum or in air for microscale x-ray analysis of several types of samples, including live organic materials. A nuclear reaction analysis (NRA) apparatus is installed at the center beam line for gamma ray detection using a CsI scintillation detector, shielded by lead for background reduction. The 15 degree right beam line is dedicated for neutron irradiations and spectroscopy and as such is heavily shielded with boron-impregnated polyethylene for neutron absorption. For this reason, ZnO films were irradiated in the 15 degree left beam line. The 30 degree right beam line is equipped with a Millatron irradiation chamber.

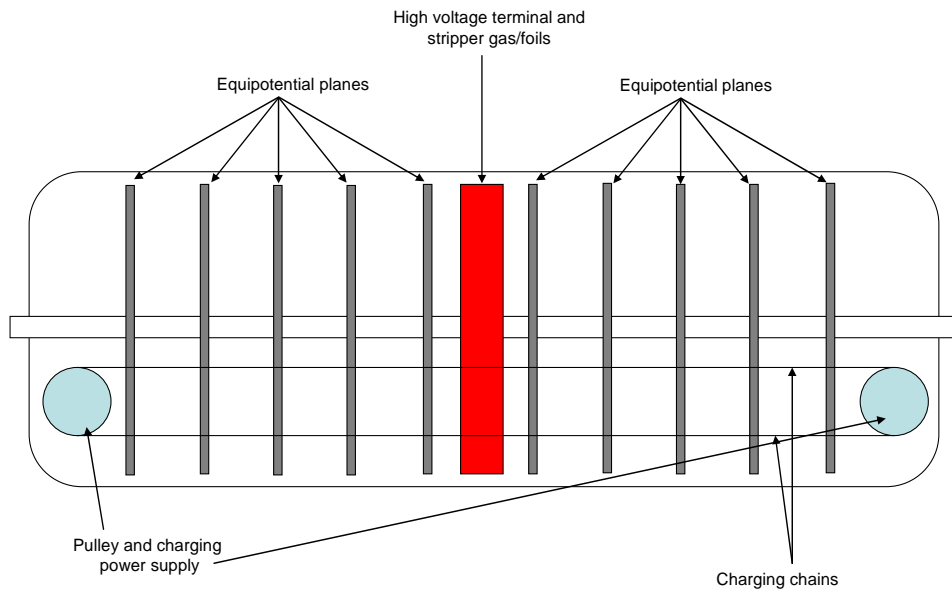


Figure 2.4 - Schematic drawing of the 3 MV tandem accelerator used at NSW Carderock Division.



Figure 2.5 - Photograph of the high-energy end of the accelerator at the PIAF. Also visible in the photograph is a set of magnetic quadrupole lenses and electrostatic steerers.

2.3.1 ^3He Irradiation of ZnO Thin Films

ZnO films were doped using the reaction $^{16}\text{O}(^3\text{He}, ^4\text{He})^{15}\text{O}$ where the product decays by beta emission to ^{15}N with a half life of 124 seconds, resulting in nitrogen acceptor impurities. The reaction has a strong cross section (167 mb) and a very broad resonance, such that the dopant density will not vary significantly across the thickness of the film. A competing reaction occurs with a cross section over 400mb, simultaneously producing an unstable isotope of fluorine by $^{16}\text{O}(^3\text{He}, p)^{18}\text{F}$ (see figure 2.6). This isotope decays with a half life of 110 minutes and so, after 30 hours, the fluorine population has decayed to one millionth of its maximum⁴.

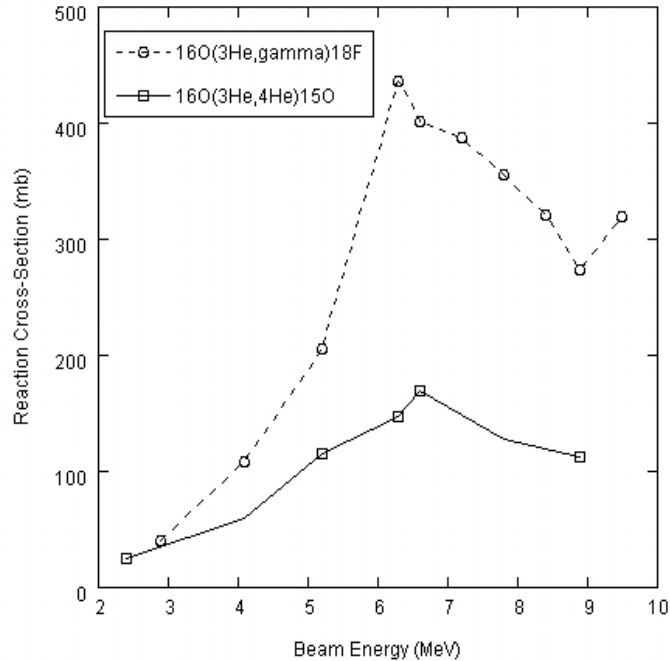


Figure 2.6 - A plot of the cross sections for the competing transmutations over from 2 to 10 MeV.

The $^{16}\text{O}(^3\text{He}, ^4\text{He})^{15}\text{O}$ reaction emits alpha particles with a predetermined energy that can be exploited to verify the transmutations in real time. The scattering chamber on the 30 degree left beam line is equipped with a solid state barrier detector positioned at 150 degrees, which is often used for Rutherford Backscattering Spectrometry. However, high levels of neutron and gamma emission required the films be irradiated in a shielded chamber and the only such chamber at the PIAF (located on the 15 degree right beam line) is not designed for particle detection. Thus, the reaction could not be monitored in real-time.

2.4 Characterization Techniques

A wide variety of characterization techniques were employed during this study, including Rutherford Backscattering Spectrometry, Nuclear Reaction Analysis, Four-

Point Resistivity probe, photo- and cathodoluminescence, atomic force microscopy and scanning electron microscopy. These methods and their specific application to these experiments are described.

2.4.1 Four-point probe resistivity measurements

Four-point probe measurements are made using four identical probes, equally spaced along the surface of the sample. A current is forced through the outer two probes while measuring the voltage across the inner two probes. Using a high-impedance voltmeter or electrometer, very little current flows through the inner probes, minimizing the contact resistance associated with the voltage measurement. Using only two-point measurements, the voltage is measured with current-carrying probes. As such, the probe and contact resistances become non-trivial.⁵

This technique is not error-free however, in the case of thin films. There are three correction factors that have to do with the geometry of the sample with respect to the probes (see equations 2.2 and 2.3). These factors compensate the measurement for proximity of the probes to an edge (F_3), lateral sample dimension (F_2) and for sample thickness (F_1). Because of the small probe spacing used in the apparatus, probe placement with respect to the sample edge can be neglected ($F_3 = 1$)⁶.

$$r = 2psF \frac{V}{I} \quad (2.2)$$

$$F = F_1 F_2 F_3 \quad (2.3)$$

For insulating substrates, F_1 and F_2 are described by equations 2.4 and 2.5.

$$F_1 = \frac{t}{s} \frac{1}{2\ln(2)} \quad (2.4)$$

$$F_2 = \frac{\ln(2)}{\ln(2) + \ln\left\{\left[\left(\frac{D}{s}\right)^2 + 3\right] / \left[\left(\frac{D}{s}\right)^2 - 3\right]\right\}} \quad (2.5)$$

For a probe spacing of 40 mils and a sample thickness of 500nm, F_2 is approximately 0.967 and $F_1=4.532t$. So, the equation for resistivity reduces to equation 2.6.

$$r = 4.382t \frac{V}{I} \quad (2.6)$$

The current apparatus consists of a Keithley 6517a electrometer, Keithley 220 programmable current source and a Lucas 302 four-point probe stand (see figure 2.6). The measurement head uses four tungsten carbide probes, spaced .040" (~1 mm) apart. The force applied by the probes on the material surface is 85 grams.

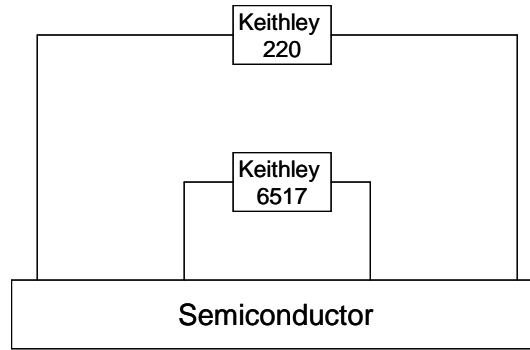


Figure 2.7 - A circuit schematic of the four-point probe apparatus with the Keithley 220 current source and Keithley 6517a electrometer.

An alternative to Hall measurements for determining the carrier concentration is to characterize the samples using resistivity measurements. Using an accepted value for mobility, one can calculate carrier concentrations from the measured resistivity according to equation 2.7.

$$n = \frac{1}{qm_n r} \quad (2.7)$$

However, the mobility of a semiconductor is important to know because it is a good indicator of crystal quality and electrical activity of dopants. Mobility can also degrade due to impurity scattering under very high dopant concentrations, but in this case is most likely to degrade from crystal damage and electrically inactive sites. Therefore, it is desirable to determine the true mobility of the sample, rather than assuming an intrinsic mobility for calculation purposes.

2.4.2 Luminescence

Luminescence measurements are useful for studying shallow impurities in electronic materials. These measurements consist of an excitation to generate carriers and a detection system to examine the luminescence emitted during de-excitation. There are many types of luminescence experiments including photoluminescence, cathodoluminescence, and electroluminescence differing largely in how carriers are excited in the material. The two forms utilized for these characterizations are photo- and cathodoluminescence.

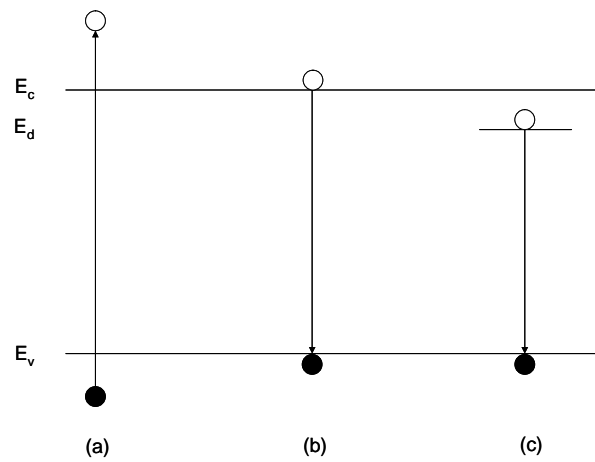


Figure 2.8 - Electronic transitions in semiconductors observed during PL experiments, including (a) photon absorption and (b) emission from band-band recombination (c) and donor-valence band recombination, such as in n-type material.

Photoluminescence utilizes lasers (typically with photon energy greater than the bandgap) to optically excite carriers in a material. The photo-generated carriers can then recombine any number of ways, including photon emission (see figure 2.7). This optical recombination can be exploited to study the electronic states in a semiconductor by examining the emission spectrum. Methods for the detection of light include a

spectrometer to disperse the light and either a solid-state array (CCD or diode) or photomultiplier tube for higher sensitivity.

Cathodoluminescence employs an electron beam controllable between 1-30 keV to generate carriers in a material. SEMs are often equipped with a CL attachment for materials characterization, in addition to x-ray detectors. The light produced by the electron beam is collected by a parabolic mirror to focus the light from the sample onto the input slit of the spectrometer, and measured by a photomultiplier tube.

In general, detection methods are similar for PL and CL. For materials with very wide band gaps, PL becomes impractical as lasers operating at sufficiently short wavelengths are either very costly or unavailable. In these situations, CL is often used. Low temperature luminescence yields further information by removing thermally excited carriers, helping to resolve states occurring at similar energies. Temperature dependent data can also be used to determine the activation energy of states near the bandgap.

In the PL measurements, a Melles Griot, 325nm HeCd laser was used for sample excitation. The luminescence was detected using an Acton Spectrapro 500 spectrometer coupled with a Princeton Instruments RY-1024 diode array, sensitive to 1400nm. For low temperature measurements, samples are cooled in a Janis 8DC dewar equipped with both sapphire and quartz windows for improved UV optical transmission.

The CL measurements are conducted using an Oxford MonoCL SEM attachment coupled to a JEOL JSM-6400 thermionic emission SEM. The MonoCL apparatus consists of a short focal-length parabolic mirror to focus the light into a monochromator. The spectrally resolved light is then detected using a liquid-cooled photomultiplier tube, sensitive from 200-900nm. The MonoCL attachment may also be operated in a

panchromatic mode, where all luminescence is counted by the PMT. This is often useful for spatially mapping the emission to features on the material surface.

2.4.3 Photoconductivity

Illuminating a sample can significantly alter the electronic properties of the sample by generating excess carriers. Photoconductivity is one such technique used to characterize this photo-response by measuring a number of parameters. The simplest form of this method simply uses polychromatic light to generate excess carriers in the sample and measure the resistivity, using a four-point probe. Other variations include studying the response to varying wavelengths of light by doing the same experiment as before, except with spectrally resolved light.

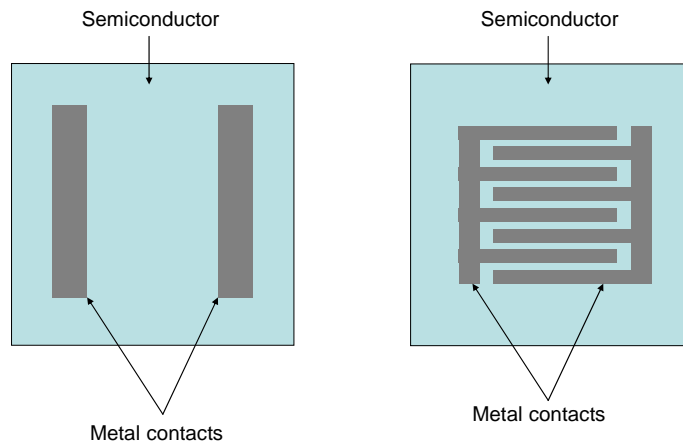


Figure 2.9 - A comparison of standard and interdigitated contacts.

One very useful variation employs interdigitated contacts where the exposed material is maximized for a certain contact separation (see figure 2.9). The photocurrent, I_{ph} , is given by equation 2.8.⁷

$$I_{ph} = Aqhf_{ph}G \quad (2.8)$$

The gain of the device is commonly defined as the ratio of the change in detected current to the change in incident optical power. Furthermore, the gain is a function of geometry, carrier mobility and lifetime and the applied bias voltage. Assuming that holes have a shorter lifetime than electrons in an intrinsic material, the gain is given by equation 2.9.

$$G = \frac{(m_n + m_p)t_p V}{L^2} = \frac{\Delta I_{ph}}{\Delta I_{photon}} \quad (2.9)$$

In an extrinsic case, one carrier is predominantly responsible for conduction and the contribution from the other is negligible. Equation 2.10 gives the gain for an n-type sample.

$$G = \frac{m_n t_n V}{L^2} \quad (2.10)$$

Thus, in both extrinsic and intrinsic cases, one can extract mobility information, assuming the carrier lifetime is known. By varying the geometry and the electric field, a linear relationship between the gain and electric field can be determined; the slope of which represents the product of carrier mobility and lifetime. Similarly, if the mobility is well known, then the lifetime can be extracted from the slope.

These equations are useful when the experiment is designed to apply an electric field to the device and measure changes in current. However, experiments have been designed to apply a bias current to the photoconductor and measure changes in voltage and conductance. Such is the apparatus used in this study, requiring modification of the above equations.

We can rewrite the expression for gain in terms of conductance and the electric field, rather than the device current, introducing the device width (W) and film thickness (t) to this expression.

$$\mathbf{J} = \frac{s\mathbf{E}}{L} \quad (2.11)$$

$$I = \mathbf{J}Wt = Wt \frac{s\mathbf{E}}{L} \quad (2.12)$$

$$\therefore \text{Gain} = \frac{\Delta I_{ph}}{\Delta I_{photon}} = \frac{Wt\Delta(s\mathbf{E})}{L\Delta I_{photon}} \quad (2.13)$$

We now set equations 2.9 and 2.13 equal to each other to form an expression for the optical gain of the photoconductor that can be used for this experimental approach.

Note that equation 2.17 is the same as before, but we have now obtained an equation for the mobility-lifetime product as a function of known parameters in equation 2.15.

$$\frac{Wt\Delta(\mathbf{s}\mathbf{E})}{L\Delta I_{\text{photon}}} = (m_n t_n + m_p t_p) \frac{V}{L^2} = (m_n t_n + m_p t_p) \frac{\mathbf{E}}{L} \quad (2.14)$$

$$Wt \frac{\Delta S}{\Delta I_{\text{photon}}} = (m_n t_n + m_p t_p) \quad (2.15)$$

$$\text{Gain} = Wt \frac{\mathbf{E}}{L} \frac{\Delta S}{\Delta I_{\text{photon}}} = \frac{\mathbf{E}}{L} (m_n t_n + m_p t_p) \quad (2.16)$$

$$\text{Gain} = (m_n t_n + m_p t_p) \frac{V}{L^2} \quad (2.17)$$

In this experiment, a Keithley 220 programmable current source is used to drive a bias current through the device and a Keithley 6517a high-impedance electrometer measures the voltage. Optical excitation is provided by means of an Oriel illuminator, equipped with a 75 W xenon arc lamp, feeding into a motor-controlled monochromator with entrance and exit slits to limit the transmitted bandwidth. The bandwidth for these measurements is 5 nm, unless specified otherwise. The monochromator stepper motor, electrometer and current source are controlled by LabView 8.0 via IEEE-488.2 GPIB connection.

2.4.4 Rutherford Backscattering Spectrometry

Ion beams provide interesting methods for characterizing and profiling chemical content over a large range of densities. One such method, Rutherford Scattering Spectrometry (RBS), typically uses protons or alpha particles to profile mass in a sample. As a particle scatters in the backward direction from a nucleus in the target, it imparts some fraction of its energy on the nucleus and keeps the remainder. The ratio of the two particle energies, or kinematic factor, is dependant on the target and impinging masses as well as the scattering angle. These kinematic factors can be easily calculated for all nuclei and allow for quick calculation of backscattered particle energies.

Since particles lose energy in a predictable way as they travel through a lattice, it is possible to quantitatively profile the constituent elements of the target. Programs such as RUMP can be used to fit theoretical spectra to experimental data, providing reasonable quantitative models to describe both the density of an element, but also a density profile over a certain thickness.

There are other methods for obtaining atomic profiles such as Secondary Ion Mass Spectroscopy (SIMS) that have much greater sensitivity, but RBS has many strengths as well; including speed, sub-surface profiling without the need for sputtering or etching and the quantitative nature of the data. The major cause for RBS being a quick measurement is that the vacuum requirements are not particularly stringent. Experiments can be done in vacuum as poor as 10^{-4} Torr. A major advantage of RBS over SIMS is that it is non-destructive. That is, bulk profiling can be achieved by RBS without the need for sputtering or etching material away from the surface like is required for SIMS. Crystallographic data can also be obtained using channeling RBS, where the target

crystal is aligned along two axes such that the incident ion beam can channel through the lattice.⁸

For example, an alpha particle beam with energy E_1 is incident on a two-layered target (see figure 2.10). At the front surface of layer 1, some particles will scatter in a backwards direction towards a particle detector (usually a Schottky barrier diode) and the energy of the particle is recorded. This energy, E_2 is dependent only on the kinematic factor and E_1 because it has scattered from the surface of the target. As the beam travels through layer 1, it slowly loses energy and as such, the energy of the backscattered particles will decrease. Energy E_3 is now a function of the E_1 , the kinematic factor for the layer and the thickness of the target through which the beam has traveled. This holds true for E_4 as well, using the appropriate kinematic factor.

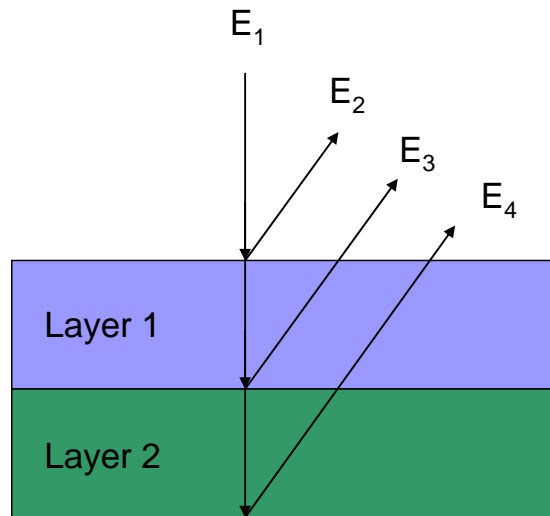


Figure 2.10 - A schematic representation of RBS analysis performed on a target composed of two monatomic layers.

If layer 1 was gold and layer 2 was silicon, both 100 nm thick, the RBS spectrum would look similar to the left spectrum shown in figure 2.10. The peak on the high-

energy (right) side is the distribution of particles backscattered from the gold layer and the other peak is from the silicon layer. The difference in backscatter energies is a result of both the thickness of the Au surface layer as well as the large difference in kinematic factors between gold and silicon. The intensity of the peaks is also due to the different scattering cross sections of gold and silicon

Now, if the target was composed of a gold-silicon compound rather than two monatomic layers of gold and silicon, the spectrum would look similar to the second spectrum shown in figure 2.11. The energy spread between the two peaks is less because the Si is now at the surface, rather than buried under 100nm of gold. The gold peak is both narrower and shorter than the previous example because there is less gold per unit volume. A lower density will produce fewer backscattered particles and a narrower peak because the incident beam experiences less energy loss before reaching the back surface of the gold layer.

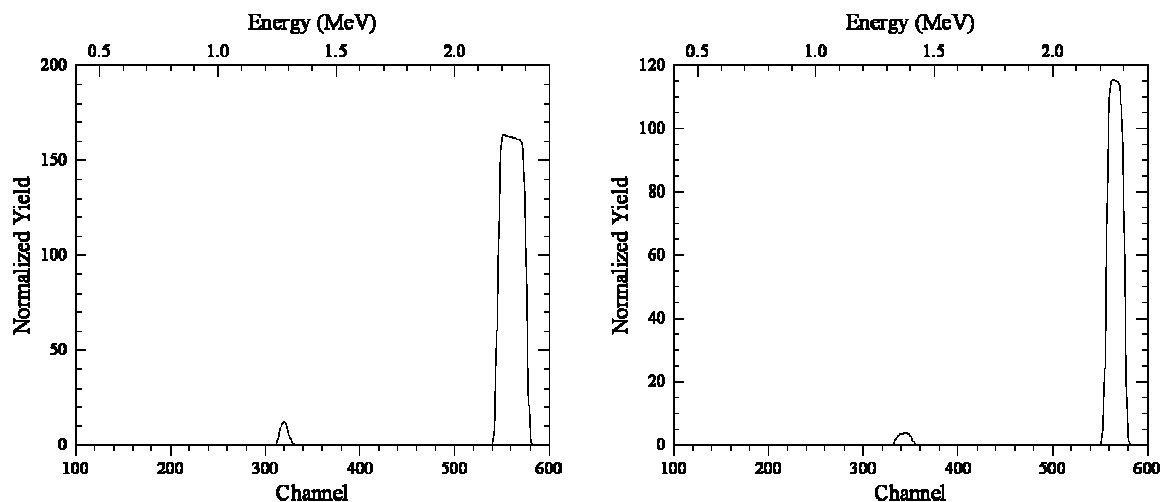


Figure 2.11 - Ideal spectra of a Au on Si target (left) and a Au-Si compound (right) using a 2.5 MeV alpha particle beam. Note that the two spectra were plotted with a different vertical scale. The spectra were simulated using RUMP, a package developed by Mike Thompson.

Since zinc has a much higher kinematic factor than the other atomic constituents in ZnO/Al₂O₃, the zinc related data in the spectrum will be separated from the other species. As such, it is straightforward to determine if zinc content in the films is changing during annealing. With careful data collection, it is possible to also distinguish the oxygen backscatter from the aluminum backscatter. As such, RBS is an excellent technique to analyze the overall quality of the films, but also to quantitatively track changes in zinc and oxygen content during annealing experiments.

2.4.5 Nuclear Reaction Analysis

RBS is an excellent tool for profiling atomic content however, it is not particularly sensitive. In practical scenarios, RBS can detect concentrations down to approximately 0.1%. For concentrations below that, another ion beam technique may be employed, called Nuclear Reaction Analysis (NRA).

NRA is a very useful method as it can detect very small amounts of a specific nucleus in a matrix. Using similar transmutation reactions as described for doping ZnO, one can probe for an impurity by observing the emitted gamma rays as the beam energy changes. In the irradiated ZnO films, the dopant is ¹⁵N which has a transmutation reaction as follows: ¹⁵N(p, gamma)¹⁶O. This reaction has a resonant nature in that the cross-section has a very sharp, intense peak at certain energies as opposed to a broader peak such as those corresponding to the ³He transmutations. This resonance occurs at 897 keV with a very strong and very narrow cross section (800 mb, 1.2 keV).

This type of profiling method lends itself very well to this experiment for several reasons. First, the nucleus being detected is a very rare isotope of nitrogen (<1% natural

abundance), which means that virtually any amount of the isotope found in the sample is due to the transmutation process. Second, the reaction parameters work out very well. The cross section is very large, making it fairly easy to detect even small amounts of ^{15}N . The FWHM of the reaction cross section is also extremely narrow, resulting in very good spatial resolution.

2.5 References

¹ J.N. Zeng, J.K. Low, Z.M. Ren, T. Liew and Y.F. Lu, "Effect of deposition conditions on optical and electrical properties of ZnO films prepared by pulsed laser deposition," *Appl.Surf.Sci.*, vol. 197, pp. 362-367, SEP 30. 2002.

² B.J. Jin, S.H. Bae, S.Y. Lee and S. Im, "Effects of native defects on optical and electrical properties of ZnO prepared by pulsed laser deposition," *Mater.Sci.Eng.B-Solid State Mater.Adv.Technol.*, vol. 71, pp. 301-305, FEB 14. 2000.

³ Helmut Foll, "3.2.2 Self-Diffusion", vol. 2005, pp. 1, http://www.tf.uni-kiel.de/matwis/amat/def_en/kap_3/backbone/r3_2_2.html

⁴ R.L. HAHN and E. RICCI, "Interactions of ^3He Particles with ^9Be ^{12}C ^{16}O and ^{19}F ," *Physical Review*, vol. 146, pp. 650-&, 1966.

⁵ D.K. Schroder, *Semiconductor Material and Device Characterizations*, New York: Wiley-Interscience, 1998, pp 2-3.

⁶ D.K. Schroder, *Semiconductor Material and Device Characterizations*, New York: Wiley-Interscience, 1998, pp 8-14.

⁷ K.K. Ng, *Complete Guide to Semiconductor Devices*, New York: McGraw-Hill, 1995, pp 394-398.

⁸ W.K. Chu, J.W. Mayer and M.A. Nicolet, *Backscattering Spectrometry*, New York: Academic Press, 1978, pp 12-13.

3 Experimental Results for ZnO

3.1.1 PLD Growth Optimization

The deposition conditions were maximized to produce resistive, smooth ZnO thin films. To this end, the O₂ partial pressure and substrate temperature were varied as shown in table 2.1. ZnO films deposited at higher O₂ partial pressure were found to be more both more resistive and have a lower RMS roughness, as measured by AFM (see figure 3.1). The films resulting in the data below were deposited at 750 °C in pressures ranging from 1 to 35 mTorr. All films were grown on c-plane sapphire. The data point corresponding to the deposition at 25 mTorr, is believed to be the result of anomalous nanostructure growth similar to that shown in figure 3.2. Defect luminescence centered near 550 nm is typically attributed to oxygen vacancies in the ZnO lattice. With increasing partial pressure, this luminescence decreases (see figure 3.3)¹.

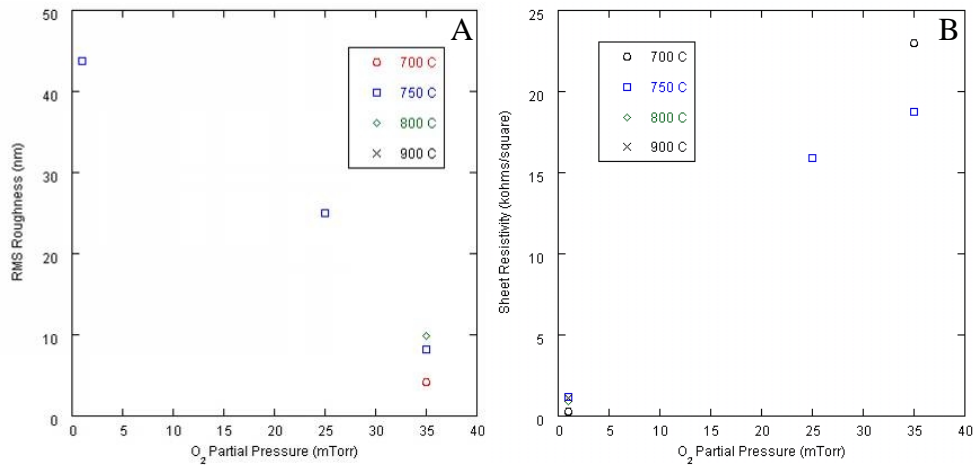


Figure 3.1 - The effects of O₂ partial pressure and substrate temperature during pulsed laser deposition on the (A) film surface and (B) resistivity.

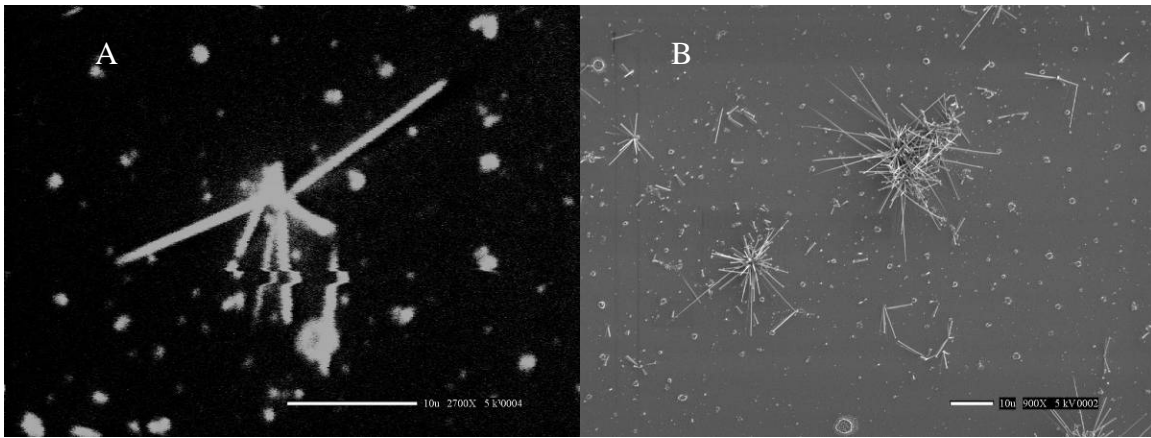


Figure 3.2 – (A) CL imaging micrograph of a collection of ZnO nanostructures and (B) SEM micrograph of anomalous nanostructure growth in ZnO thin films deposited by PLD. The film was grown at 900 °C. Bright cathodoluminescence was also observed from the ZnO nanowires.

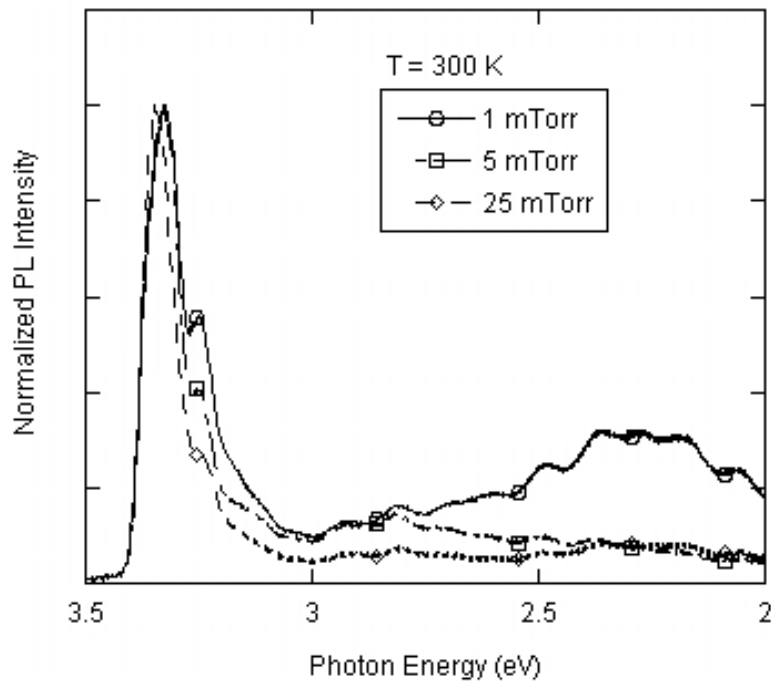


Figure 3.3 - Photoluminescence spectra demonstrating the decreased defect luminescence with respect to increasing O₂ partial pressure. This luminescence is typically associated with oxygen vacancies.

Optimal ZnO films were deposited at 700 °C, as suggested by previous studies, using rocking curve data to demonstrate the temperature dependence (see figure 3.4).² A series of depositions carried out at 1 mTorr, but substantially higher temperatures

demonstrated significant nanostructure growth, with the most prominent structures being observed at 900 °C. In this series, resistivity increased strongly with temperature as did surface roughness. In conclusion, the highest quality films were deposited at 700 °C and 35 mTorr O₂ partial pressure.

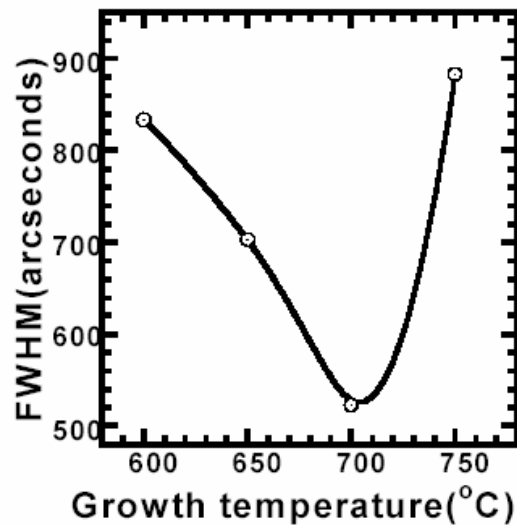


Figure 3.4 - FWHM of XRD for as-grown ZnO films as a function of deposition temperature (from Cai, et al).

3.2 Annealing of ZnO Thin Films

3.2.1 Time Dependent Annealing

Following deposition, the films were annealed to observe annealing behavior and optimize annealing conditions to increase the resistivity and smoothness of ZnO films. This first annealing study was carried out to determine the optimal annealing time for a film using an in-air quartz tube furnace at 800 °C.

3.2.1.1 Four-Point Probe

The resistivity of one film was studied using the four-point probe method after cumulative annealing times of 3, 6 and 40 hours. It was observed that the peak resistivity was nearly achieved after the first 3 hours and continued annealing only produced marginal changes in resistivity. The data may be misleading as it is believed that the four point probe stand has a non-insignificant leakage current. The equivalent internal resistivity of the apparatus was measured to be on the order of 10 k Ω -cm, which may cause the asymptotic behavior as the film resistivity approaches the internal resistance. However, if the data is valid, then the rapid change in the electronic properties of the film may indicate that the intrinsic defects in the as-grown crystal are relatively unstable or highly mobile.

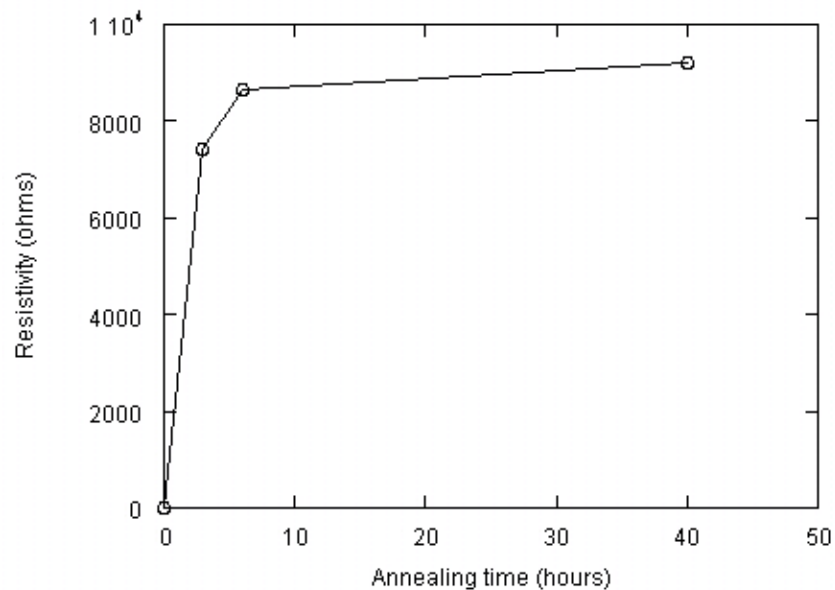


Figure 3.5 - Plot of resistivity versus cumulative annealing time

3.2.1.2 Atomic Force Microscopy

To further characterize annealing behavior, the surface was analyzed using AFM. As-grown films did not demonstrate a clearly oriented surface (see figure 3.6), but after a 3 hour anneal, the film immediately demonstrated some c-axis orientation, as indicated by the hexagonal structure. However, X-ray diffraction data from previous growths under similar conditions showed diffraction only along the (0001) direction. Further annealing again produced only a marginal change in the surface (see figure 3.7). After 6 hours total, the hexagonal grains appeared to increase in size, indicating a 2-dimensional recrystallization of the surface. After 15 hours, smaller grains begin to appear, which may reflect a vertical recrystallization of the film.

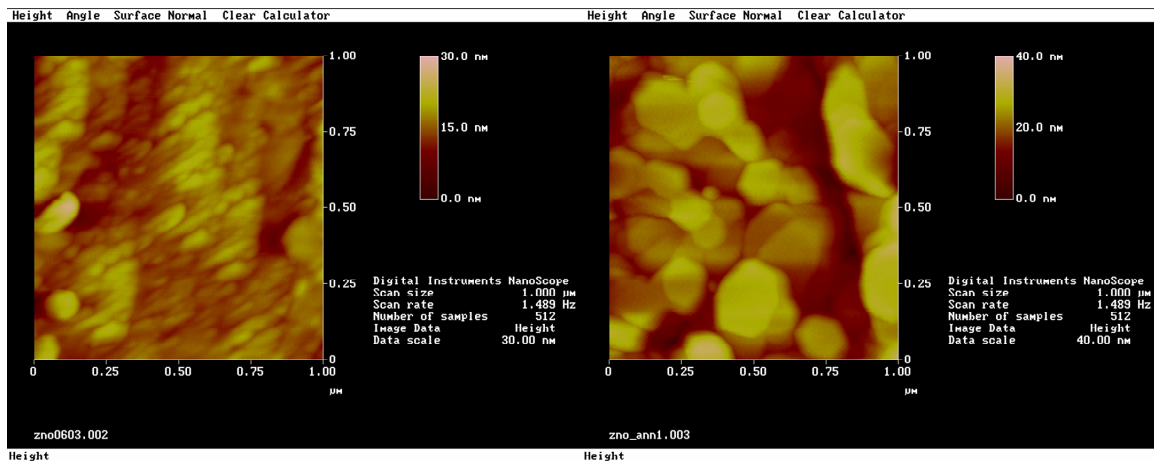


Figure 3.6 - AFM micrographs depicting the crystal orientation observed after a 3 hour (right) anneal of a ZnO film, compared to the as-grown surface (left).

The RMS roughness increased after the first anneal, which is expected from the significant change in surface structure and crystal orientation, but decreased with continued annealing (see figure 3.8).

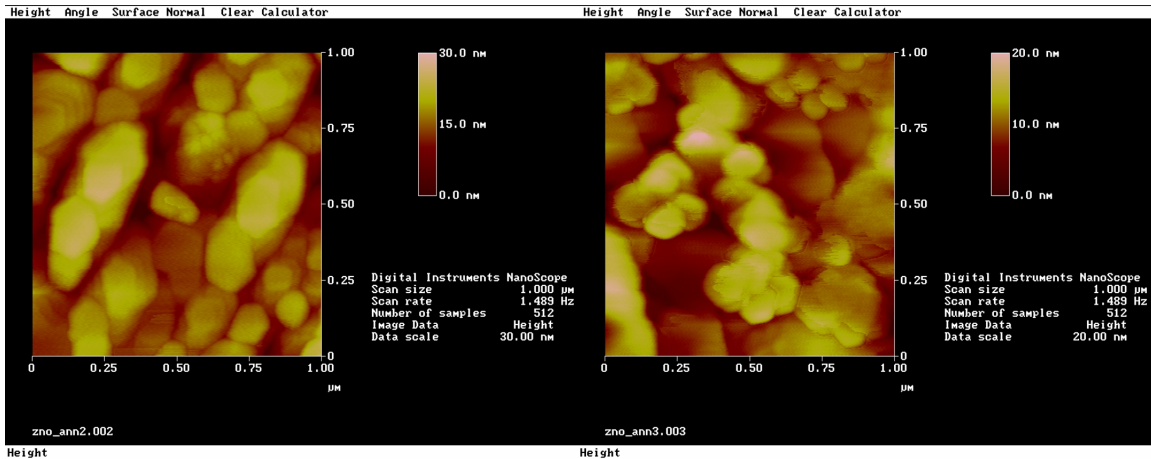


Figure 3.7 - AFM micrographs showing the film surface after 6 hours (left) and 15 hours (right) total anneal.

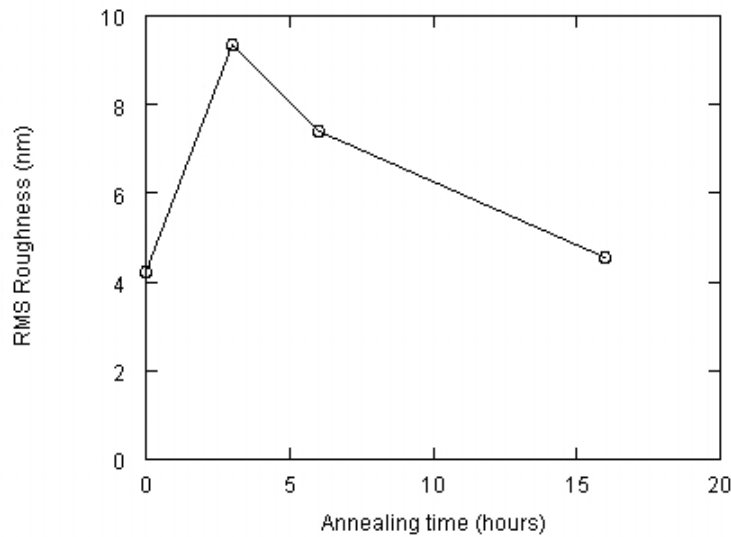


Figure 3.8 - RMS roughness of a ZnO film after successive anneals in air.

3.2.1.3 Rutherford Backscattering Spectrometry

RBS data provides information regarding the concentration of elements within the target and has been utilized to determine bulk chemical properties of the ZnO films at different stages of annealing. This method has revealed that annealing significantly

improves film stoichiometry near the surface, but extreme annealing times can cause decomposition of the film near the surface and into the bulk material (see figure 3.9). The samples were rotated to give the films a larger apparent thickness and thus, increase resolution, provided the films are thin enough. In some cases, this rotation causes different peaks to overlap as the material appears thicker, causing greater energy loss.

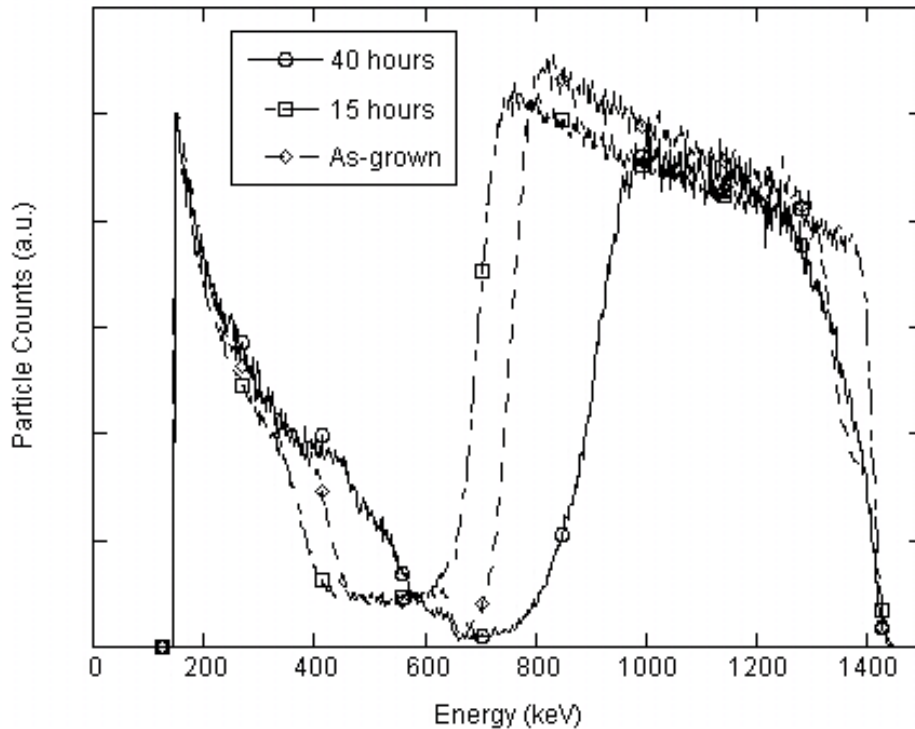


Figure 3.9 - RBS spectra of 3 films: one as-grown, one annealed 15 hours and the other annealed 40 hours. The spectra were taken using a -45 degree incident beam angle and a 150 degree scattering angle.

The as-grown film demonstrates a zinc deficient surface, but good structural film quality as both front and back edges of the zinc peak are abrupt and steep. The break in the front edge indicates a rapid change in zinc concentration with respect to depth into the material. After 15 hours of annealing, the film stoichiometry is ideal and demonstrates perfect structure, again evidenced by crisp front and back edges of the zinc peak. The

thickness of the film and the 45 degree incident angle make the Zinc data overlap with the oxygen peak. 40 hours of annealing clearly decomposes the film as the thickness of the Zinc peak in the spectrum is substantially reduced. This is further supported by the Al peak moving further up in the spectrum. The film surface also appears to be very low quality as demonstrated by a gradual tail at the back of the Zinc peak.

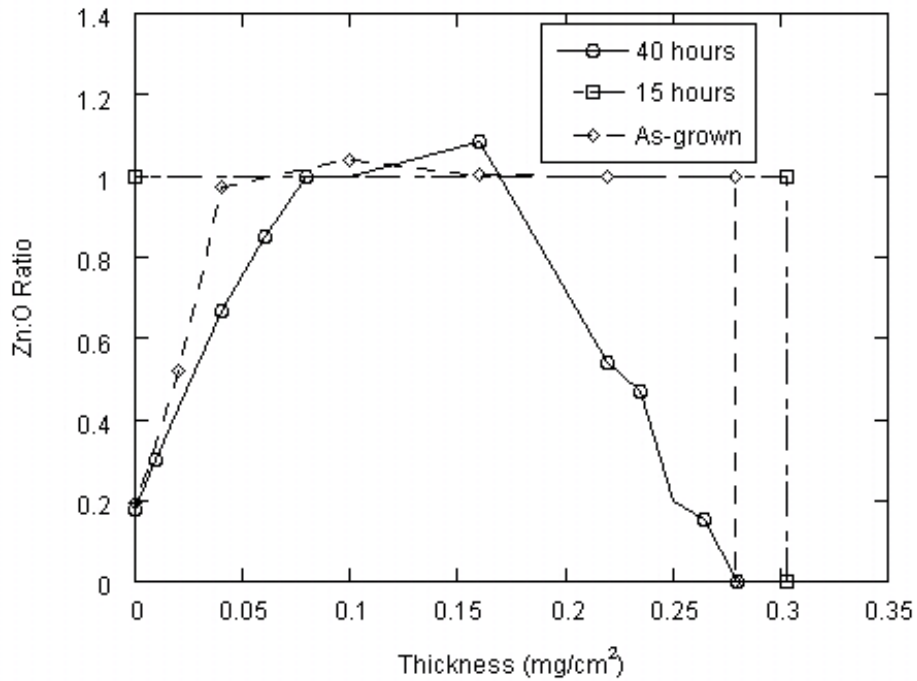


Figure 3.10 - Stoichiometry profile for three ZnO films as a function of depth. The stoichiometry was calculated using the output of an RBS analysis program.

An RBS analysis program was utilized to extract stoichiometry profiles for the films. The results indicate again that the as-grown film is oxygen rich at the surface, but achieves stoichiometric balance in the bulk material. After 15 hours, the film demonstrates a perfect Zn:O ratio throughout the film. The surfaces are also very good quality as evidenced by abrupt changes in the ratio. Again, the 40 hour anneal destroys the film stoichiometry, creating an oxygen rich film throughout most of the material and

the quality is poor, indicated by the gradual changes in stoichiometry (see figure 3.10). The reason for the different depths is because the analysis is performed using units of mass per unit area rather than length. This eliminates the variable of density, which is difficult to account for given the varying stoichiometry observed in some films.

3.2.2 Temperature-Dependent Annealing

A series of films were annealed for 2 minutes each in a rapid thermal annealing furnace (RTA) at 300, 450, 600, 750 and 900 °C in dry air. The annealed films were subsequently characterized using four-point probe, AFM, RBS, HIBS and cathodoluminescence techniques. The observed changes seem markedly smaller than those reported in the literature for similar times. A future study should utilize longer annealing times to enhance the observed effects.

3.2.2.1 Resistivity

The annealed films became more resistive with increasing annealing temperatures up to 600 °C, except for one film annealed at 450 degrees. At 750 and 900 °C, the films became conductive (see figure 3.11). It is possible that at the higher temperatures the film surface becomes Zinc rich, as oxygen is driven out by diffusion mechanisms.

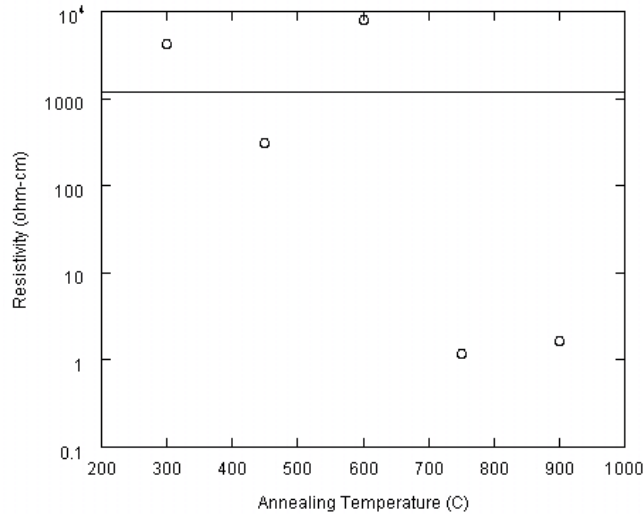


Figure 3.11 - Plot of film resistivity against annealing temperature. At high temperatures, films become highly conductive. The unannealed resistivity is shown as a solid line for reference.

3.2.2.2 Atomic Force Microscopy

AFM measurements showed increasing surface roughness among the annealed films up until 900 °C (see figure 3.12), where the film demonstrated some sort of recrystallization, resulting in ordered, periodic structure. This suggests that continuing to increase the temperature helps accelerate annealing mechanisms on or near the film surface rather than there being a temperature threshold above which films begin to anneal. Perhaps at even higher temperatures, the films would continue to improve in surface quality, as well as structure.

Similar effects were observed in films annealed at 800 °C for varying times. After 3 hours, the surface had shown signs of recrystallization, despite a substantially rougher surface than the as-grown film. With continued annealing, the surface became smoother while maintaining the oriented surface structure. In this instance, higher

annealing temperatures seem to be analogous to longer annealing periods with respect to the onset of surface recrystallization.

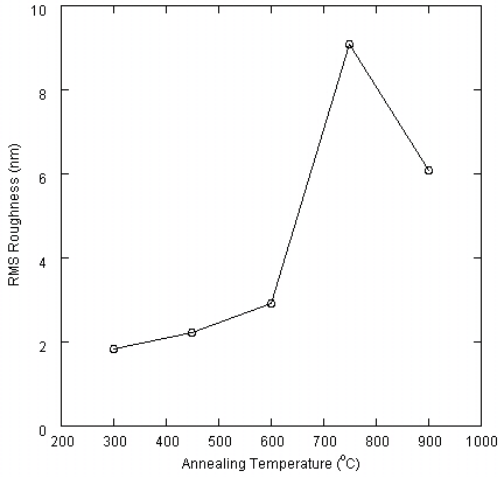


Figure 3.12 - RMS roughness for ZnO films annealed at varying temperatures.

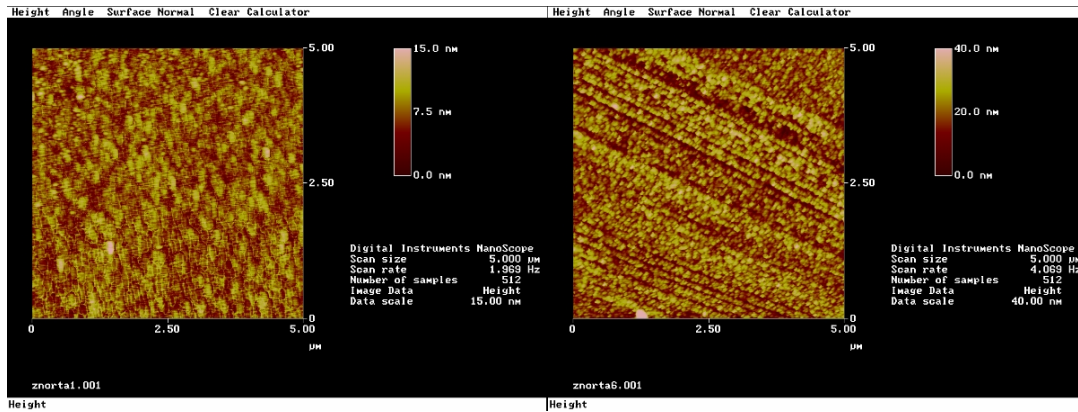


Figure 3.13 - AFM images comparing two annealed films. One was annealed at 300 °C (left) and the other at 900 °C (right). Note the sharp change in surface morphology at the higher annealing temperature.

3.2.2.3 Rutherford Backscattering Spectrometry

RBS spectra were obtained for the thin films using a combination of ion beams.

The first experiment used a 6.575 MeV alpha particle beam to exploit a significant

enhancement in the nuclear scattering cross-section for alpha particles on ^{16}O . This gives a higher resolution and better counting for analysis of the ^{16}O content near the surface of the film as a function of annealing. A sample RBS spectrum for one thin ZnO film illustrates the enhanced ^{16}O backscatter yield for this beam energy. The peak is narrow and skewed towards the high-energy side because of the narrow width of the cross-section enhancement. The backscattered particle counts for Zinc and Al are labeled for reference (see figure 3.12). The second experiment used an 8.113 MeV ^{15}N beam to enhance the depth resolution for particles scattering from a heavy nucleus, such as zinc. This technique is a variation of RBS and is often referred to as heavy ion backscattering spectrometry (HIBS).

The data shows some change in the oxygen content of the annealed films (see figure 3.13). Due to the small thickness of the films (~80-100 nm) only the first three channels, or data points, where the counts begin to increase would correspond to the oxygen content in the film, as opposed to the substrate. The difference between the spectra for the films is likely caused by a small amount of play in the rotation of the sample, and not necessarily by any change in the distribution of oxygen. This is because the front edge of the oxygen backscatter yield occurs at the same energy for all spectra. Also note the peak counts for the film annealed at 300 °C occurs at a lower energy than the rest. This indicates that the sample was tilted further away from the detector which means that detected particles would travel a longer path before leaving the film, thus losing more energy in the process.

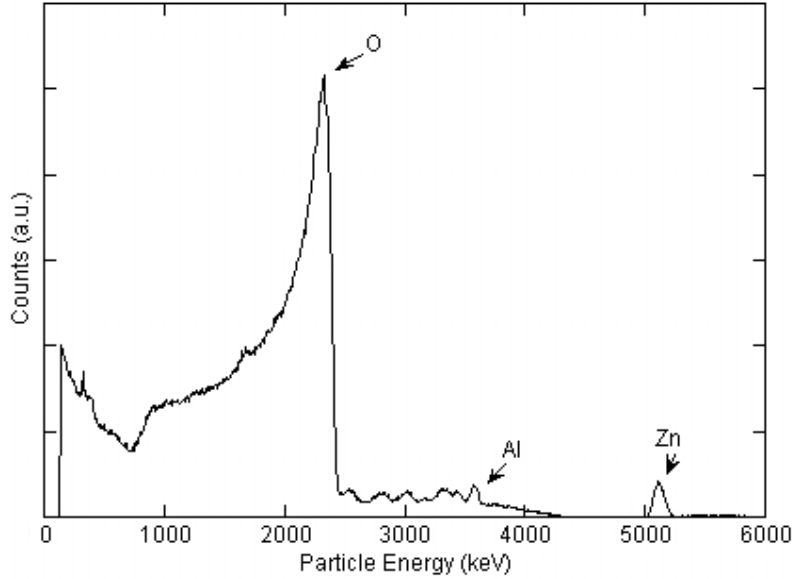


Figure 3.14 - Sample RBS spectrum from a thin ZnO film used in the RTA study. The narrow width of the oxygen peak is caused by a very narrow scattering cross-section enhancement for 6.575 MeV alpha particles on O.

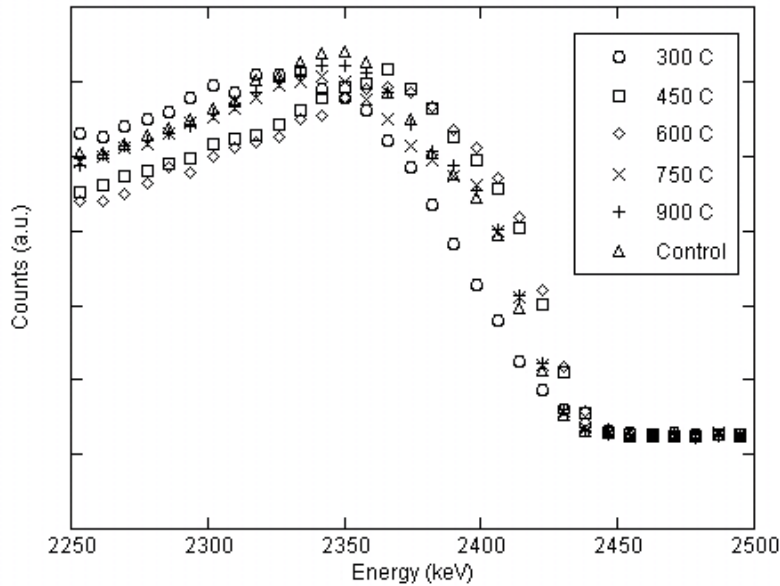


Figure 3.15 - RBS spectrum detailing the variation in oxygen content among the annealed films.

The zinc backscatter yield also shows only a minor change, but confirms that the 300 °C annealed film was taken at a slight angle. One interesting feature is the isotopic resolution of the experiment. Zinc has five stable isotopes, including ^{64}Zn , ^{66}Zn and ^{68}Zn

which each have a natural abundance of 48.06 %, 27.9 % and 18.8 %, respectively. The mass dependence of the backscatter energy explains why different isotopes can be observed by RBS, but the small difference in kinematics means that isotopic resolution is only achieved at higher projectile energies. In this case, the two most common isotopes, ^{64}Zn and ^{66}Zn , are observed in approximately the right ratio. Backscattered particles from ^{68}Zn are difficult to resolve from those scattered by ^{66}Zn because the abundances are relatively similar.

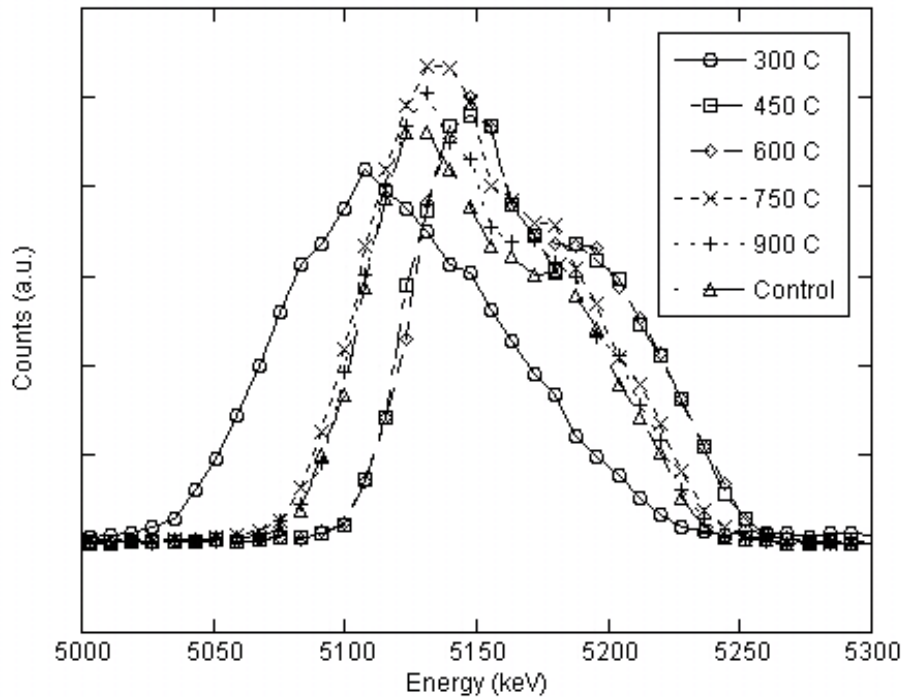


Figure 3.16 - RBS spectra showing the detail of the higher energy particles which have scattered from various isotopes of zinc.

Nitrogen scattering data showed similar results to those observed with the alpha particle beam. The RTA process has had little, if any, effect on the atomic profiles of the films (see figure 3.15). The spectra also confirm the thin nature of the ZnO films.

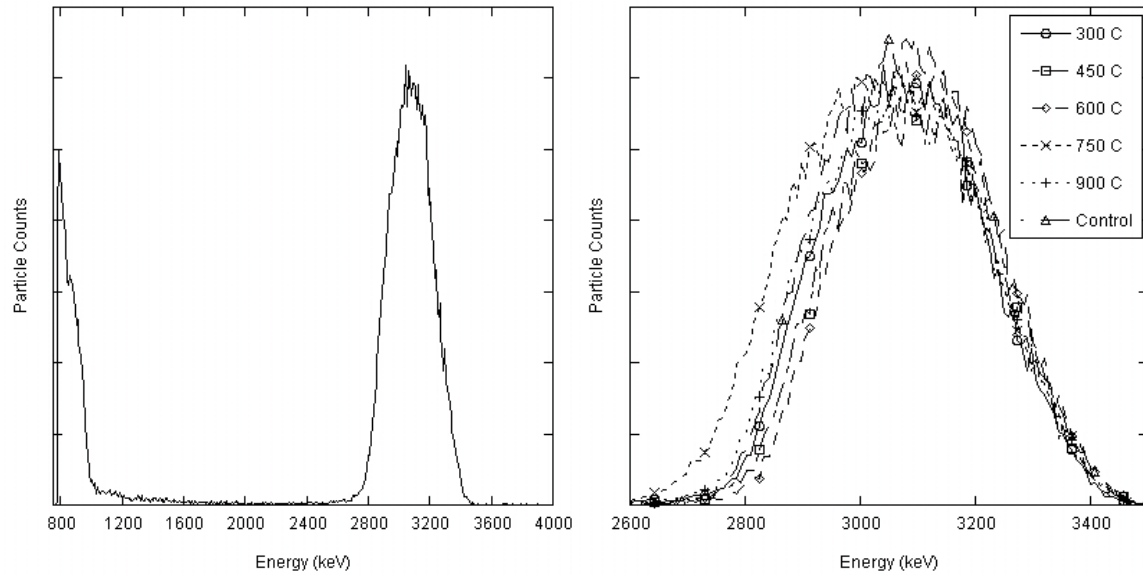


Figure 3.17 - Nitrogen-beam HBS spectra of (a) a sample annealed film to show the general energy spectrum of backscattered particles and (b) the annealed films and one control film for comparison. The spectra were taken using an 8.113 MeV ^{15}N beam with a scattering angle of 170 degrees and the sample rotated -30 degrees to increase the apparent thickness of the films.

3.2.2.4 Luminescence

Room-temperature cathodoluminescence experiments reveal that band-edge emission increases substantially with rapid anneals at 750 and 900 °C, along with increased defect luminescence (see figure 3.15). These results suggest that large-scale annealing of the film is not observable for short anneals below 750 °C, but that defect production also accompanies the improved macroscopic structure. These defects may have been the result of the RTA process itself, whereas a slower, longer anneal at similar temperatures may not produce such defect states.

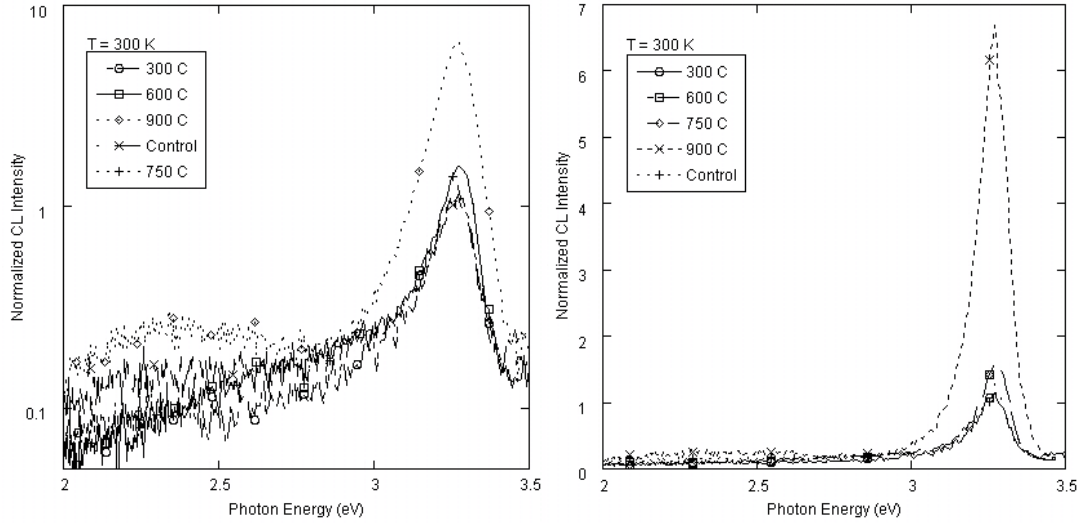


Figure 3.18 - Semi-log and linear plots of CL spectra showing increases in band-edge and defect state luminescence as a result of high temperature rapid thermal annealing.

3.3 ³He Irradiation of ZnO Thin Films

Five ZnO films were irradiated with 6.6 MeV ³He ions at the PIAF for several hours, with doses ranging from about 8 to 17 mC. These doses result in an estimated dopant concentration of approximately 1 to 3x10¹⁴ cm⁻³ (see table 3.1). Irradiated films were then characterized by SEM, AFM, cathodoluminescence, photoconductivity and resistivity measurements.

Table 3.1 - Irradiation data and estimated dopant density for five ZnO films, including total dose and average beam on target (BOT).

Film	Dose (mC)	Beam Density (nA/cm ²)	Avg BOT (nA)	¹⁵ N (cm ⁻³)
ZnO_0803	8.55	6.4941	531	2.52E+14
ZnO_0804	8.86	4.7809	421	2.38E+14
ZnO_0809	12.2	4.8654	577	3.04E+14
ZnO_0810	9.84	3.1500	617	1.18E+14
ZnO_0812	17.1	7.2158	988	2.98E+14

3.3.1 Scanning Electron Microscopy

Scanning Electron Microscopy was used to examine the irradiated films. It was found that the irradiated area appeared darker in SEM micrographs (see figure 3.17), but since the images were taken using a 5 keV electron beam, the microscope probes only a very shallow depth of the film (roughly 200nm). As such, this darkening is indicative of a change in the film and not caused by implantation damage in the substrate.

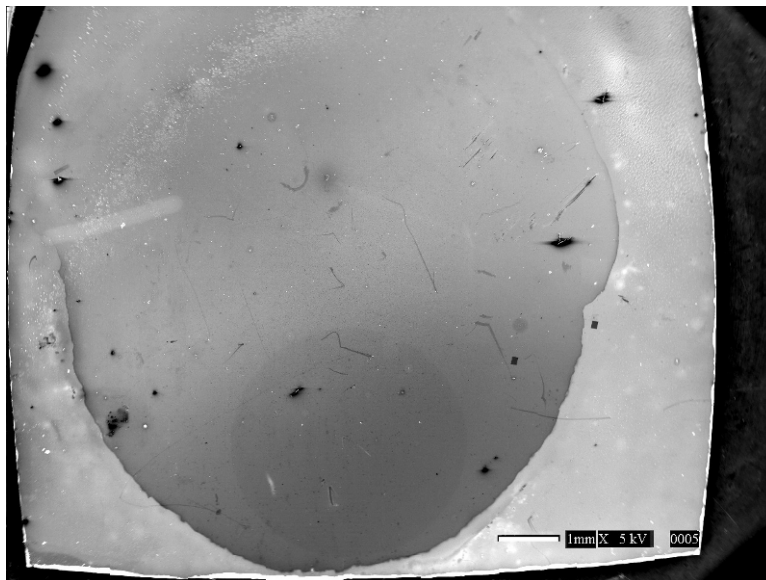


Figure 3.19 - SEM micrograph of an irradiated ZnO film. The darker region corresponds to the irradiated portion of the film.

Two things could lead to the contrast observed in the image: electronic change in the ZnO film, altering the secondary electron (SE) emission or a mass change in the film, altering the backscattered electron (BSE) yield. The electronic change could simply be a change in conductivity associated with the ion beam interactions. A more insulating material will hold charge at the surface, causing the image to be either lighter or darker

for accumulation of negative or positive charge, respectively. The change in mass, possibly due to surface contamination, would alter the BSE yield since it varies strongly with mass. It is possible that carbon could have contaminated the irradiated surface due to the heat or energy deposited by the ion beam, similar to carbon contamination observed in SEMs. The thin, lightweight carbon film would cause the irradiated surface to appear darker because it decreases the BSE yield compared to that of pure ZnO.

Micron sized circular features were observed on some of the irradiated films and across the entire surface of one such film, ZnO_0810 (see figure 3.18). To further study the nature of the features, a diamond scribe was used to lightly scratch the film surface and the damaged features were observed in the SEM. The micrographs indicate that the structures have collapsed entirely as opposed to simply fracturing which suggests the features were hollow or gas-filled rather than solid ZnO material which may have expanded. A CL image of one feature, taken at 320 nm, demonstrates that there is no remaining ZnO film beneath the collapsed structure. That particular emission wavelength was chosen because sapphire has a defect state that emits near 320 nm which cannot be confused with any ZnO emission. A similar CL image was taken of the same feature at 1 keV to demonstrate that there is no significant ZnO film remaining on the substrate where the feature used to exist. The range of the electron beam through ZnO at 1 keV is 10-15 nm.

Radiation blistering was observed in a previous study where amorphous materials were implanted with MeV-range hydrogen or helium ions. The study reported that there is a minimum critical dose required for blister formation and further suggests that the blisters are created by ion beam induced stresses. These stresses cause the hydrogen or

helium ions to migrate towards the surface, forming bubbles underneath the surface, which causes blister-like features. This process is well illustrated as it occurred in 100 keV N implanted GaAs thin films that were subsequently annealed. As the ions coalesce at the interface between the substrate and the film, they form bubbles or gas pockets, applying a pressure on the surface film which causes the film to separate in some places from the substrate.³

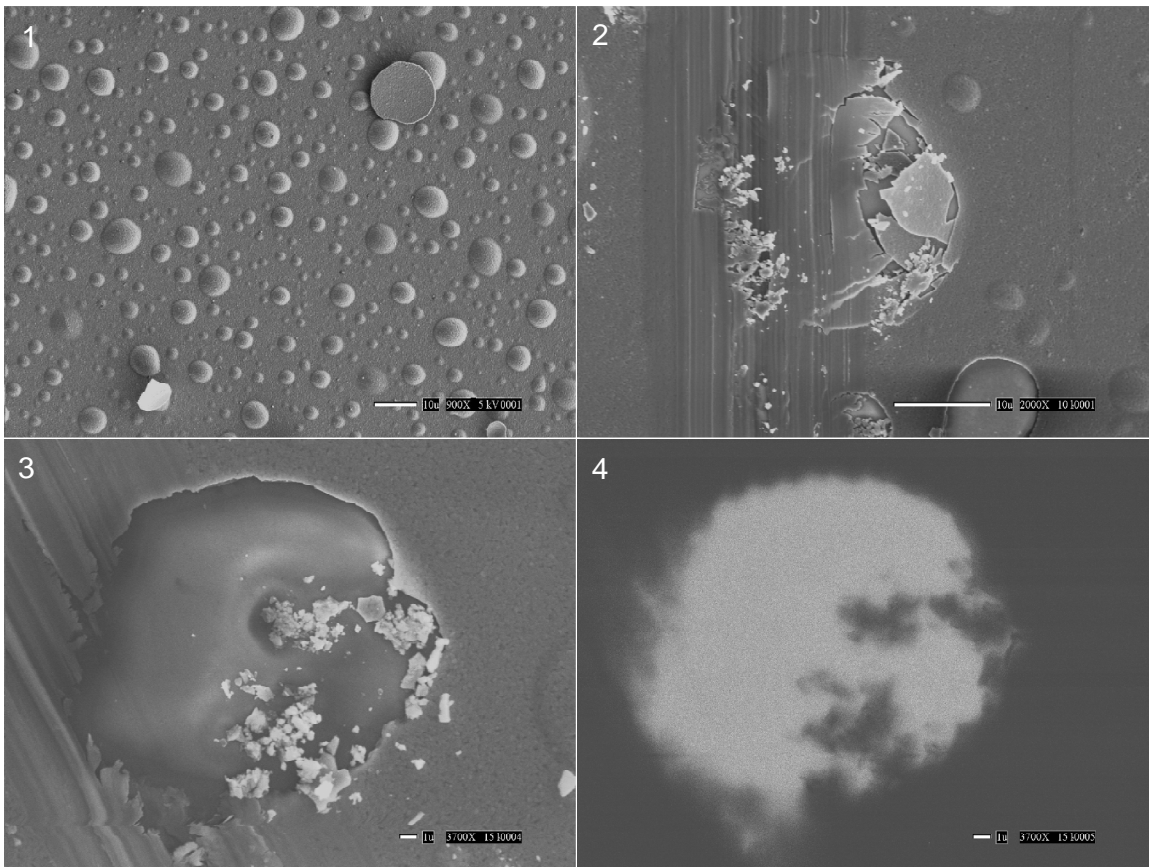


Figure 3.20 - SEM micrographs of blisters formed on a ZnO film (1), a blister that has collapsed after scribing (2 and 3) and a CL image taken at 320 nm of a collapsed blister.

This does not explain why or how blisters would have formed on regions of the surface that were not exposed to the ion beam. Furthermore, the formation of blisters is not readily correlated to the observed increase in film resistivity. However we have

previously noticed that if a very zinc-rich target is used, the films produced will sometimes delaminate over time with a progression of circular type areas. It is our suspicion that the helium gas is gathering specifically in these areas forcing them up into a bubble shape.

3.3.2 Luminescence

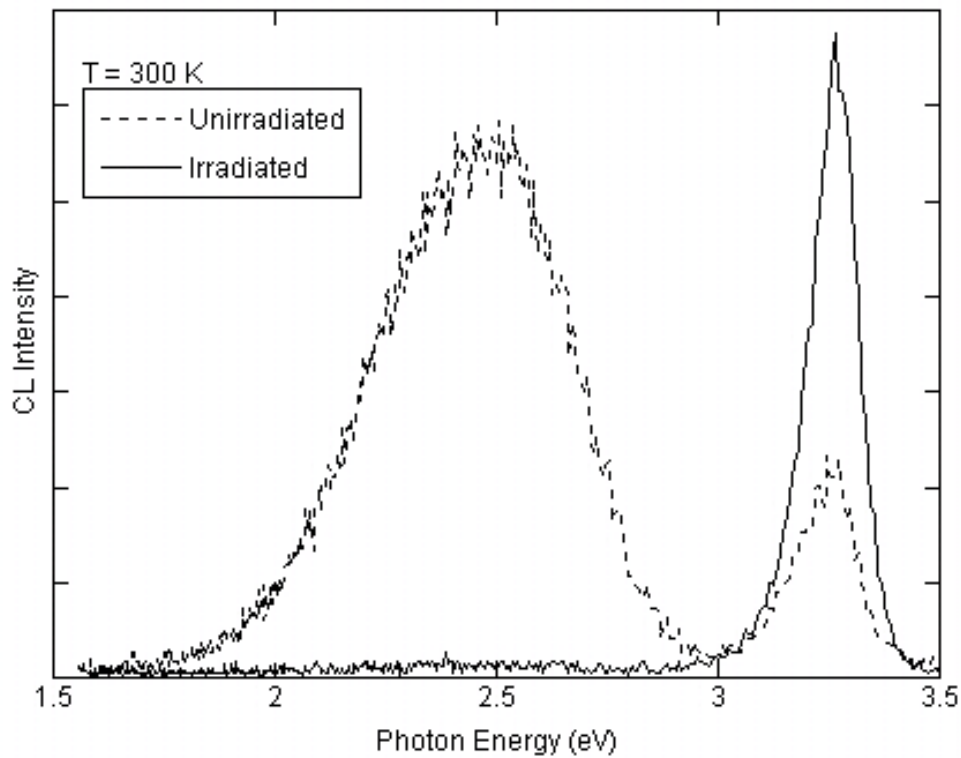


Figure 3.21 - Room temperature CL spectra depicting the annealing properties of the ^3He ion beam. The spectra were taken on the same film, using irradiated and unirradiated regions for a direct comparison.

Irradiated films were studied using cathodoluminescence to observe changes in defect energies and band structure. The irradiated films were found to have a significantly reduced defect luminescence compared to the unirradiated control samples in the irradiated region of the film (see figure 3.19). The fact that this effect did not occur

over the entire film indicates that this is likely a direct result of beam interactions and not a bulk thermal process.

3.3.3 Resistivity

The change in CL emission between the irradiated and unirradiated portions of the films indicated a possible annealing effect specifically caused by interactions of the ion beam with the sample. This was further investigated by four-point resistivity probe. Resistivity measurements taken at the center of the film were on the order of four to ten times higher than those taken in the unirradiated portions. The resistivities measured in the unirradiated portions were also similar to control films which had not been irradiated. This further suggests that the ion beam annealing is directly related to beam-sample interactions rather than thermal annealing caused by the deposition of energy into the film.

The fact that higher resistivities are observed in the irradiated portions suggest that the darkening observed in the SEM micrographs is due to electronic change, more so than surface contamination caused by the irradiation. Since the darker portion is more resistive, it will accumulate more charge per unit area than on the more conductive area, both deflecting the electron beam and affecting the secondary electron yield. As positive charge accumulates on the film surface, ejected electrons (backscattered and secondary electrons) must overcome a certain electric field in order to reach the detectors of the SEM. The secondary electrons are very dependent on this charge build-up because of their low energy. As the positive charge increases, fewer and fewer secondary electrons have enough energy to escape the attractive surface of the film. The opposite scenario

occurs for negative charge accumulation, where the image is brighter because more secondary electrons are able to escape the repulsive film surface.

3.3.4 Atomic Force Microscopy

Irradiated films showed a substantial decrease in surface roughness compared to the unirradiated films (see table 3.2). The typical RMS roughness, as measured by the AFM for a 5x5 μm scan, was approximately 36 nm and 18 nm for the unirradiated and irradiated films, respectively. There was one irradiated film that still showed as rough a surface as before irradiation. It is possible that this film was rougher than average to begin with since control films were used to achieve proper comparisons. Also note that ZnO_0810 is the film entirely covered in blisters, and that these would exaggerate the roughness of the true film surface. AFM scans illustrate the improvement in the film surfaces after irradiation, agreeing with the roughness measurements (see figure 3.20). One possibility for this effect is the sputtering of tall peaks above the surface, though this is not likely to occur due to the reduced beam scattering encountered at such high energies. A possible alternative is that the restructuring of the surface is result of sample heating, effectively annealing the irradiated surface. No strong correlation could be found between the surface roughness and any of the irradiation parameters listed in table 3.1. However, it should be noted that sample ZnO_0803 received the smallest total dose, but only marginally over other films that demonstrated a lower RMS roughness.

Table 3.2 - RMS roughness for irradiated and unirradiated films.

Film	RMS Roughness (nm)
Control 1	36.434
Control 2	38.139
ZnO_0803	36.120
ZnO_0804	18.969
ZnO_0809	15.437
ZnO_0810	18.202
ZnO_0812	19.972

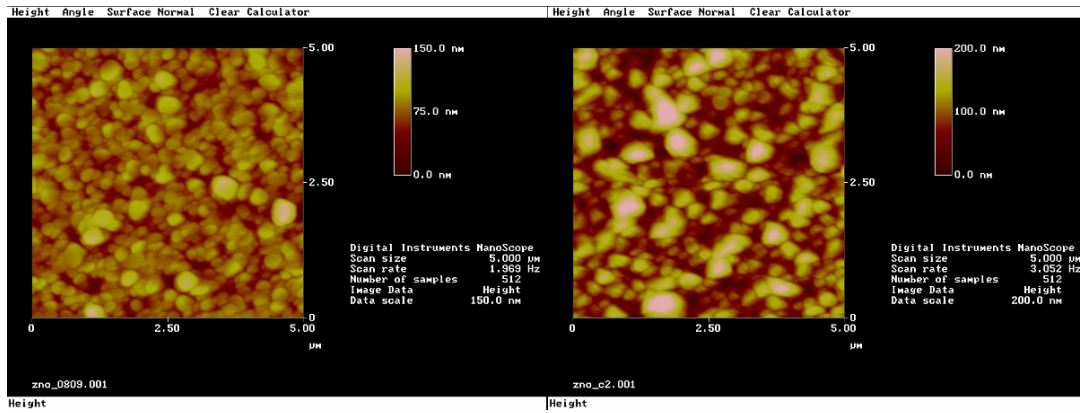


Figure 3.22 - 5x5 μm AFM scans of (a) an irradiated film and (b) a control film. Note the difference in the z-range of the scan.

3.3.5 Photoconductivity

To study the photoconductive properties of the ZnO films and their behavior after annealing, photoconductive detectors were fabricated by depositing 200 nm thick aluminum contacts on the film surface in an interdigitated configuration. The interdigitated fingers were spaced 3, 5, 10 and 20 microns apart to observe changes in the gain of the device with respect to geometry (see figure 3.20).

Dark and illuminated current-voltage (I-V) curves show a significant increase in resistivity in irradiated films as compared to unirradiated films. This increase is in strong agreement with four-point resistivity measurements. Illumination of the photoconductive detectors was achieved by means of a small mercury lamp, which

provides strong UV excitation. Not only were the irradiated films more resistive under dark conditions, but they were much more responsive to the illumination as well (see figure 3.22a-b). This trend was confirmed by spectrally resolved photoconductivity measurements (see figure 3.22c). Note the sharp increase in UV photoresponse of the photodetector.

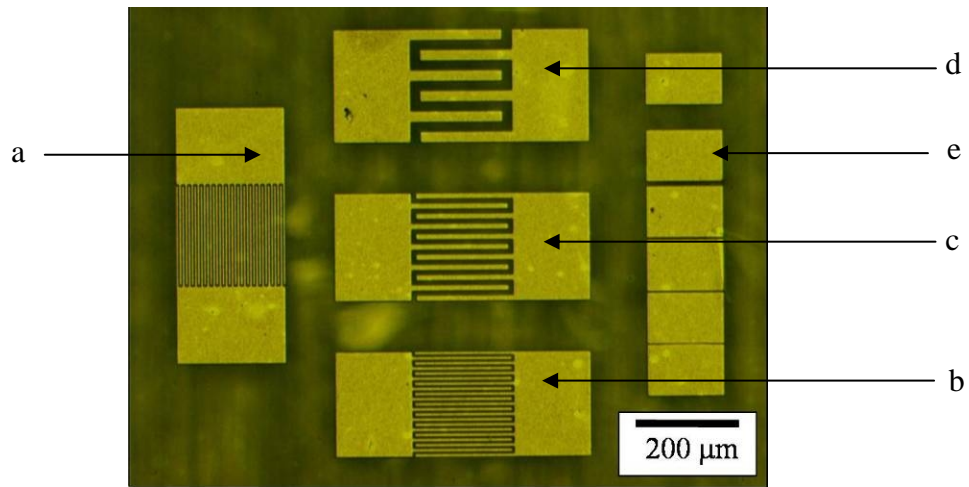


Figure 3.23 - Optical micrograph of the interdigitated structures fabricated on ZnO films. The finger spacings are (a) 3, (b) 5, (c) 10 and (d) 20 microns. A TLM structure (e) was also patterned onto the films with contact spacings of 2, 3, 5, 10 and 50 microns.

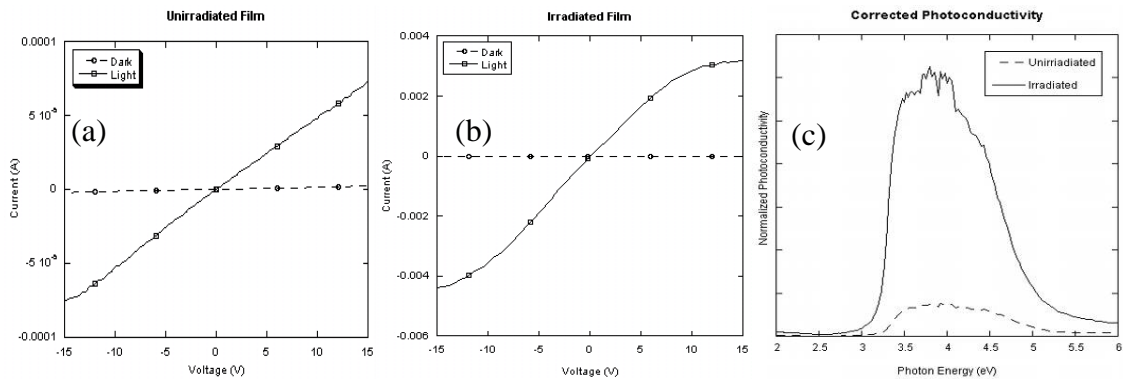


Figure 3.24 - Current-voltage curves confirm increase in resistivity and illustrate the increase in the electronic response to UV excitation of (a) unirradiated films compared to (b) irradiated films. Spectrally resolved photoconductivity measurements are shown in (c). Note the spectrally resolved photoconductive data has been corrected for the spectral dependence of the lamp irradiance.

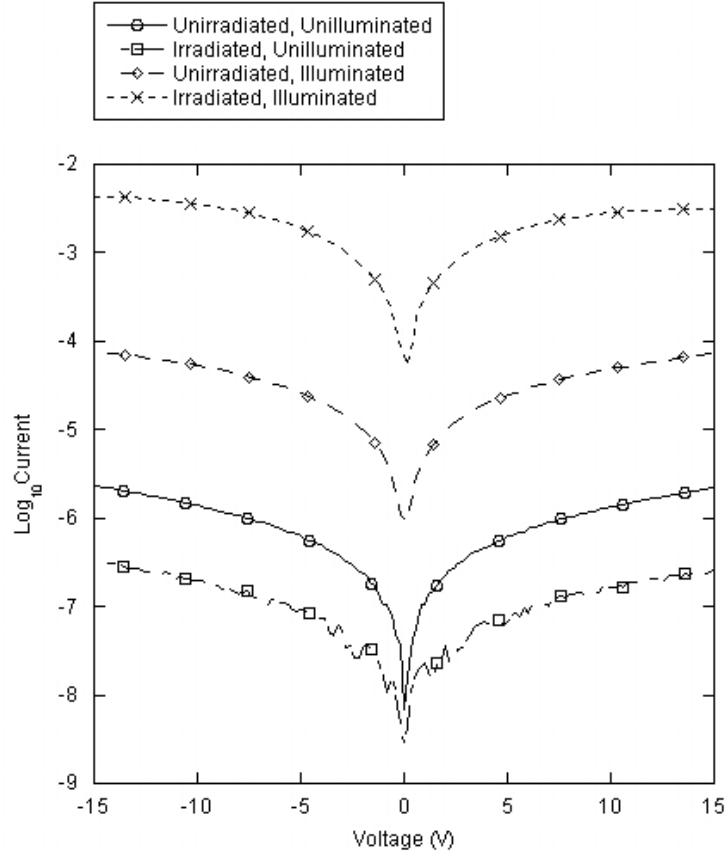


Figure 3.25 - Log(Current) versus Voltage plot showing the response over several orders of magnitude of the control and the irradiated samples to illumination from a mercury lamp.

The contrast between light and dark currents through the photodetectors improved drastically after irradiation (see figure 3.23). The control sample demonstrated a contrast ratio of about 10:1, compared to the irradiated sample which was over 10^4 :1 – an improvement of 10^3 . Note again the increased dark resistivity of the irradiated sample compared to that of the control sample. The substantial increase in the contrast ratio may in fact be the result of incorporation of nitrogen into the ZnO lattice. Sources have reported that doping of photoconductive materials can often increase the photosensitivity of the material.^{4,5}

Persistent photoconductivity was also observed in these films. To characterize this effect, spectrally-resolved photoconductivity apparatus and software was modified to record the time response to modulated light. The monochromator was set to 378 nm with a 5 nm spread in wavelength at FWHM.

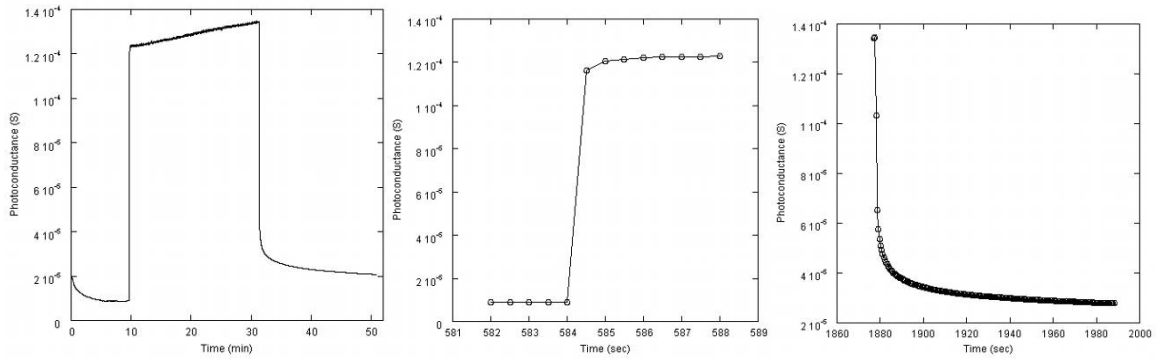


Figure 3.26 - Persistent photoconductivity (a) effects observed in irradiated ZnO films. The (b) growth and (c) decay of the conductance are expanded to show more detail.

The behavior observed in figure 3.24a is characteristic of trapping. As the shutter was opened, allowing light incident on the film surface, excess electrons and holes are generated and quickly reach equilibrium. The time it takes to reach equilibrium is generally limited by the carrier lifetimes, but that is not the case for this experiment since the light was modulated by hand using a shutter. Thus, the rise time is limited by the modulation rate of the light source, which is substantially slower than either carrier lifetime. Once equilibrium is reached, trapping effects begin to dominate the time response of the system, resulting in a slow, linearly increasing photoconductance. As the light source is shuttered, the decay mechanisms can be observed much more clearly than the growth mechanisms (see figure 3.24b), due to the very slow decay rates (see figure

3.24c). The two-stage decrease in conductance is due to the rapid recombination of excess carriers followed by the slow emptying of filled traps.⁶

The persistent photoconductivity effects observed in this brief experiment are not uncommon in ZnO, but require future study. Continued experimentation would provide a better understanding of the complex behavior of trapping centers in ZnO and how this behavior might be altered by ion beam irradiation and nuclear transmutation.

3.4 References

¹ B.J. Jin, S.H. Bae, S.Y. Lee and S. Im, "Effects of native defects on optical and electrical properties of ZnO prepared by pulsed laser deposition," *Mater.Sci.Eng.B-Solid State Mater.Adv.Technol.*, vol. 71, pp. 301-305, FEB 14. 2000.

² A. L. Cai, J. F. Muth, M. J. Reed, H. L. Porter, C. Jin, and J. Narayan, "*Effect of growth temperature and annealing on ZnO*," presented at Quantum Confined Semiconductor Nanostructures, Dec 2-5 2002, Boston MA, United States, 2002.

³ X. Weng, W. Ye, R.S. Goldman and J.C. Mabon, "Formation and blistering of GaAsN nanostructure layers," *J.Vac.Sci.Technol.B*, vol. 22, pp. 989-992, MAY-JUN. 2004.

⁴ R.H. Bube, *Photoconductivity in Solids*, New York: John Wiley and Sons, 1960, p 171.

⁵ H.L. Porter, A.L. Cai, J.F. Muth and J. Narayan, "Enhanced photoconductivity of ZnO films Co-doped with nitrogen and tellurium," *Appl.Phys.Lett.*, vol. 86, pp. 2119-2121, MAY 23. 2005.

⁶ R.H. Bube, *Photoconductivity in Solids*, New York: John Wiley and Sons, 1960, pp 273-284.

4 Conclusions

ZnO continues to be the subject of substantial interest for use in UV and visible LEDs and lasers, as well as solar-blind UV photodetectors and thin film transistors. The main hurdle to widespread production of such devices is the difficulty in producing reliable, high quality p-type ZnO material. This has forced the development of novel and innovative methods for producing p-type ZnO films and homostructures.

Recent studies have produced p-type ZnO doped with nitrogen, lithium, arsenic, and phosphorus as well as arsenic and antimony within the last few months. These materials consistently demonstrate reduced mobilities as compared to intrinsic films, even for low dopant densities. It was the goal of this study to investigate the production of quality p-type nitrogen-doped ZnO films by nuclear transmutation. While the amount of nitrogen incorporated in the film was not quantified, various characterizations were utilized to determine its effects and any side effects of the irradiation process.

4.1 Pulsed Laser Deposition of ZnO Thin Films

It was determined that higher quality ZnO films could be prepared by PLD at high O₂ partial pressures and that the optimal substrate temperature was near 700 °C, according to a previous study. The criteria were based on photoluminescence, resistivity and AFM studies which all showed, that increasing the partial pressure from 1 to 35 mTorr consistently produced smoother, more resistive films with better luminescence properties.

4.2 Annealing of ZnO Thin Films

Excessive annealing periods (40 hours) at 800 °C in air caused substantial film degradation, as measured by RBS. This was apparent from the wildly varying film stoichiometry, as well as the backscatter properties of the surface and interface. Shorter (8 hour) anneals proved to be very beneficial to film stoichiometry and maintained abrupt backscatter features, indicative of a smooth, uniform surface and interface. As-grown films were shown to be oxygen-rich at the surface, becoming stoichiometric further into the film.

Rapid thermal annealing for 2 minutes in air at varying temperatures did not reveal substantial information. Rather, it demonstrated that such short anneals have a very limited effect on the distribution of zinc and oxygen in the lattice. Also, the surface was shown to recrystallize at high enough temperatures for the short anneal. This suggests that the onset of recrystallization is not activated by some threshold temperature, rather that higher temperatures accelerate this and similar annealing mechanisms. This study also showed significant increase in visible luminescence in films annealed above 750 °C, possibly suggesting that the film is undergoing defect-inducing stresses during higher temperature anneals. However, these anneals also lead to substantial increases in near-band edge luminescence, implying that the overall film quality is improving.

4.3 ³He Irradiation of ZnO Thin Films

Bombardment of the films with ³He ions has caused substantial improvements in several film characteristics, including resistivity, luminescence and photoconductivity.

Irradiated films, as compared to virgin films, demonstrated approximately a four-fold increase in resistivity, presumably caused by defect annealing during the irradiation process but the possibility for low levels of defect compensation is still considered. Visible luminescence was substantially decreased in irradiated films with little or no sign of impurity related luminescence. This with the resistivity data supports the theory that the ion beam is annealing the donor-like point defects in the ZnO films. Photoconductivity measurements show that irradiated films possess a much higher UV photoresponse than do the control films. A contrast ratio of 10^4 was observed for irradiated devices – nearly a factor of 10^3 better than for control devices. This is not the result of a four-fold increase in resistivity, but rather of a more complex change in the irradiated films. Perhaps it is the result of incorporation of nitrogen into the ZnO lattice.

These all indicate an improvement in overall film quality and a reduction in mid-gap defect states which was not necessarily expected from the irradiation process. Thus far, no measurements have conclusively indicated the existence of nitrogen acceptors in any ZnO film, though this is at least partly caused by the low dopant concentrations. If nothing else, ^3He irradiation of ZnO films may prove to be an effective method for the annealing of point-defects.

4.4 Considerations for Future Work

This study has shown that ^3He irradiation of ZnO films improves film and device characteristics. However, this creates several possibilities for future studies including further analysis of currently irradiated samples, ion-beam annealing of new samples and

transmutation of new samples using a higher output accelerator or longer irradiation times.

At this point, to understand what has happened in these films at these low concentrations requires further characterization. Such analysis should include photo- or cathodoluminescence at near liquid helium temperatures to observe emission from any acceptor-bound exciton states or donor-acceptor-pair recombination. Substantial emission from these processes was not readily observed at the temperatures achieved in this study. Another technique that could be employed is positron annihilation spectroscopy to determine if the donor-like point defects are being annealed by the ion beam, or if they are being compensated by nitrogen acceptors.

Irradiation of ZnO films should be studied using other ion beams to determine annealing was largely caused by ^3He ions or one of the reaction products such as alpha particles, protons, ^{15}O , ^{18}F or positrons from the isotope decay. A comprehensive study should also include experiments to determine if there is an energy or dose dependence on the extent or efficiency of the annealing process.

If it is possible, ZnO films should be irradiated for a longer period of time or using a higher output accelerator to increase dopant concentrations by at least an order of magnitude. This could improve results from the techniques employed in this study and would also enable the use of SIMS or NRA methods to detect nitrogen levels in the lattice.